HYDROLOGY OF CONTAMINANT FLOW REGIMES TO GROUNDWATER, STREAMS, AND THE OCEAN WATERS OF KĀNEʻOHE BAY, OʻAHU

THESIS SUBMITTED TO THE GRADUATE DIVISION OF THE
UNIVERSITY OF HAWAIʻI AT MĀNOA IN PARTIAL FULFILLMENT
OF THE REQUIREMENTS FOR THE DEGREE OF

MASTER OF SCIENCE
IN
GEOLOGY AND GEOPHYSICS
AUGUST 2018

By
Michael R. Mathioudakis

Thesis Committee:

Craig R. Glenn, Chairperson
Henrietta Dulai
Aly I. El-Kadi
Robert B. Whittier

ACKNOWLEDGEMENTS

First and foremost, I would like to thank my advisor Craig Glenn for envisioning and funding this project, and providing sound scientific mentorship while allowing me the opportunity to explore my interests therein. I would like to thank Hawai‘i Sea Grant for the funding to complete this project, as well as funding and support from the University of Hawai‘i Water Resources Research Center, the Hawai’i State Department of Health, and a graduate student research grant from the Geological Society of America. I would also like to thank and acknowledge the Honolulu Board of Water Supply, the Hawai‘i Commission on Water Resources Management, and the community of Kahalu‘u for helping coordinate access to groundwater wells used in this study.

I would like to thank Daniel Dores for his partnership on this project. This project has been an adventure, and it has been a great pleasure having a true friend and colleague to share it with. Field work for this project was made possible by contributions from Trista McKenzie, Daniel Litchmore, Eric Welch, and Krissy Remple, all of whom I am indebted to.

I would like to thank my parents for an unparalleled primary education, and for constantly encouraging me to follow my dreams. Annual family vacations to the Atlantic Ocean cultivated in me a fascination for the ocean that led me to this pursuit, and for that I am forever grateful.

Last but not least I would like to thank my support system, starting first and foremost with my wife Mikayla, who has been my rock for the past eight years as I have pursued my dreams. My siblings Lexi, Jonathan, Timothy, and Kristina have been by my side for all of life’s challenges and championships, and they inspire me to be the best that I can be -- for this I am extremely grateful. I thank my lifelong friends in Indiana for always pushing me to be the best I can be, and my dear friends and fellow grad students in the Geology and Geophysics ‘ohana for making this two-year roller coaster an adventure to remember.

This research was supported by grants (C. Glenn, PI) from the Hawai‘i Department of Health, the U.S. Geological Survey State Water Resources Research Institutes Program, and a grant/cooperative agreement from the National Oceanic and Atmospheric Administration, Project R/WR-2, which is sponsored by the University of Hawai‘i Sea Grant College Program, SOEST, under Institutional Grant No. NA14OAR4170071 from NOAA Office of Sea Grant, Department of Commerce. The views expressed herein are those of the author and do not necessarily reflect the views of NOAA or any of its subagencies. UNIHI-SEAGRANT-XM-16-02.

ABSTRACT

Study focus:

Groundwater is an important source of nutrients for coastal waters, but can act as a pathway for anthropogenic contaminants to reach the ocean. On the Hawaiian Island of Oʻahu, nearly 1500 on-site sewage disposal systems (OSDS; e.g., cesspools and septic tanks) exist within the Kāneʻohe Bay drainage basin, releasing one million gallons of untreated wastewater into the groundwater each day, threatening stream and coastal water quality. This study evaluated hydrologic flow paths from OSDS to surface water bodies by utilizing a combination of unmanned aerial vehicle thermal infrared imaging (UAV-TIR), stream gauging and seepage runs, and numerical groundwater modeling.

New hydrological insights for the region:

This study found that approximately 1.12×10^7 m^3 of groundwater is directly entering the ocean each year, primarily in the form of diffuse submarine groundwater discharge with significantly elevated concentrations of all major nutrients. Eight groundwater seep locations were identified by UAV-TIR, with all seeps occurring through coastal valley fill or beach sediments. Model results confirmed that valley fill, which extends as deep as 425 meters in some locations, is the most hydraulically conductive substrate in the study area, with hydraulic conductance 16x greater than dike-intruded basalt. This is a marked contrast to many other coastal settings on Oʻahu, where valley fill deposits act as a semi-confining barrier to groundwater flow through the aquifer.

Table of Contents

List of Tables

List of Figures

1.0 INTRODUCTION

On-site sewage disposal systems (OSDS, e.g., cesspools and septic tanks) are the third leading cause of groundwater contamination in the United States, and are a particular concern in tropical islands where OSDS exist in close proximity to drinking water wells, streams, and coastal waters (Babcock et al., 2014). Over 110,000 OSDS exist in the state of Hawai‘i, 88,000 of which are cesspools (Hawai‘i State Department of Health, 2015). Approximately 53 million gallons of untreated wastewater are discharged from cesspools into the groundwater each day in Hawai‘i, releasing a nitrogen load of approximately 12,000 kilograms per day, along with fecal bacteria and other wastewater constituents (Whittier and El-Kadi, 2009). Potential human health hazards associated with OSDS include gastrointestinal infections (Novello, 2000; Said et al., 2003; Hrudey and Hrudey, 2007), methemoglobinemia (Knobeloch et al., 2000), and death (Novello, 2000). Numerous studies throughout the Hawaiian Islands have shown sewage-derived nitrate is likely responsible for increases in both native and invasive algae over-production (Dailer et al., 2010; Dailer et al., 2012; Amato et al., 2016), but the subsurface fate and transport mechanisms of these contaminants is relatively unknown. Understanding where and how OSDS contaminants reach drinking water wells, streams, and coastal waters is essential for land managers and legislators to plan and prioritize infrastructure upgrades and wastewater management policy. Thus, the purpose of this study is to delineate contaminant flow paths from OSDS to surface water bodies (i.e., streams and the ocean) and drinking water wells in the Kahalu‘u region of O‘ahu, Hawai‘i, where over 900 OSDS exist within a 24 km^2 area.

Whittier and El-Kadi (2009) completed an inventory and human health risk ranking of all OSDS in Hawai‘i (Kahalu‘u inventory provided in **Table 1**), and Babcock et al. (2014) completed a condition assessment of OSDS, finding that 32% of OSDS in Hawai‘i are failing or in danger of failing. The Hawai’i State Department of Health completed monthly surface water monitoring in Kahalu‘u from 2014-2016, finding levels of fecal bacteria Enterococcus well in excess of EPA standards. In 2017, the Hawai‘i legislature passed Act 125, which requires replacement of all cesspools in the State by 2050, and directs the Hawai’i State Department of Health to evaluate cesspools statewide to identify those that require immediate upgrade due to human and/or environmental health risk (Hawai‘i State Department of Health,

2017). Kahaluʻu, on the eastern coast of the island of Oʻahu (**Figure 1**), is one of two areas in the State of Hawaiʻi designated as Cesspool Upgrade Priority Level 1, meaning that cesspools in the area pose "Significant Risk of Human Health Impacts, Drinking Water Impacts, or Draining to Sensitive Waters" (Hawaiʻi State Department of Health, 2017).

Table 1: Inventory of on-site sewage disposal systems (OSDS) in the Kahaluʻu region of the Kāneʻohe Bay watershed. Cesspools, which lack a treatment component and account for 72% of the OSDS in the study area, have the highest predicted nitrogen concentrations (Whittier and El-Kadi, 2009).

OSDS Class	Effluent Nitrogen (mg/L)	No. Units	Units / km²
Class I (Soil treatment)	1	194	8
Class II (Septic)	36	27	1
Class III (Aerobic)	24	20	1
Class IV (Cesspool)	60	666	28
Multiple	45	16	1
TOTAL	**46**	**923**	**39**

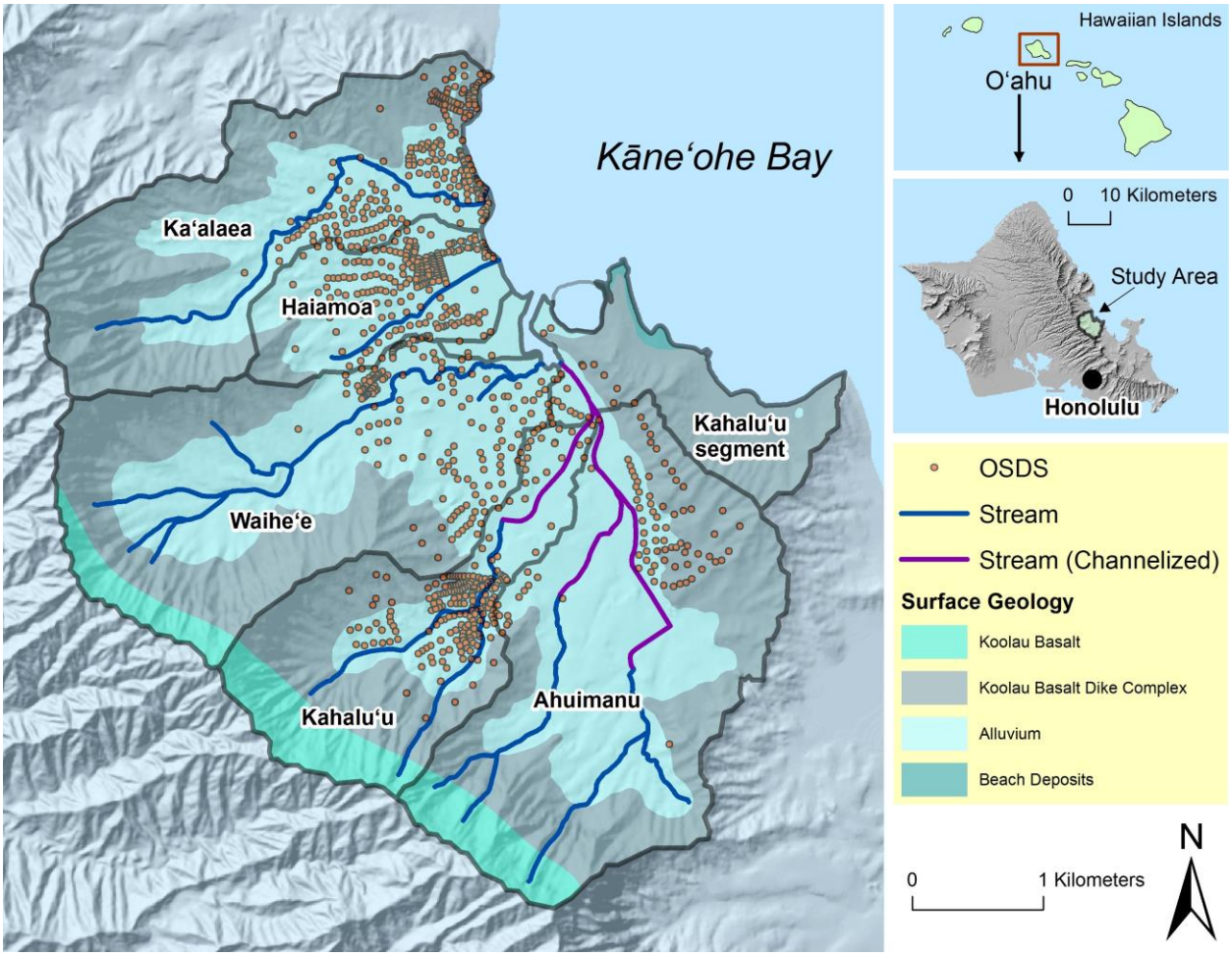

Figure 1: Map of the Kahaluʻu study area showing major sub-watersheds, streams, and distribution of on-site sewage disposal systems (OSDS). Nearly two-thirds of all OSDS in the Kāneʻohe Bay drainage basin are located within the study area watersheds. Surface geology (after Sherrod et al., 2007) in and around all major streambeds is primarily alluvium, while the ridgelines consist primarily of interbedded lava flows intruded by volcanic dikes (Macdonald et al., 1983; Takasaki and Mink, 1985; Walker, 1986; Walker, 1987; Izuka et al., 2015). As shown, 87% of the OSDS in the region are located within the alluvium, and thus the hydrogeological characteristics of this geologic layer act as primary controls on contaminant transport.

In order to test the hypothesis that groundwater is transporting OSDS contaminants to surface waters, this study employs a full hydrologic analysis of the Kahalu‘u area to delineate subsurface contaminant flow paths. Groundwater inputs to streams are quantified with stream seepage runs, and submarine groundwater discharge (SGD) locations are mapped with unmanned aerial vehicle thermal infrared (UAV-TIR) imaging. Nutrient concentrations are analyzed for all suspected groundwater discharge locations, and compared to baseline concentrations. A numerical groundwater model is used to simulate subsurface transport of OSDS contaminants, and simulated model concentrations of dissolved inorganic nitrogen (DIN) are compared to measured groundwater DIN concentrations for model validation. As legislators and land managers plan and implement future infrastructure and wastewater management policy, this study provides a framework that is replicable in coastal areas worldwide that are impacted by anthropogenic groundwater contamination.

2.0 REGIONAL AND HYDROLOGIC SETTING

The Island of Oʻahu is the third largest island in the Hawaiian Island chain, and is home to nearly 70% of the State of Hawaiʻi's population (United States Census Bureau, 2016). Oʻahu is comprised of the 3-4 Ma Waianae and Koʻolau shield volcanoes that have both undergone denudation by weathering and massive volcanic flank area slumping (Moore et al., 1989, 1994), and which are currently in the post-shield stage of development (Macdonald et al., 1983). The study area is located on the windward side of Oʻahu, bordered by Kāneʻohe Bay to the northeast and the Koʻolau Mountains to the southwest (Figures 1 and 2). Stemming from the central Koʻolau caldera located immediately southeast, a northwest striking rift zone of dense vertical dikes extends throughout the basalt bedrock of the study area. Heavy orographic rainfall on this windward side of the island persists throughout most of the year, and numerous perennial streams traverse very steep topographic gradients, especially in the northern portion of Kāneʻohe where the Koʻolau peaks exceed 800 meters within a few kilometers of the coast. Deep weathering and erosion of the Koʻolau headlands has resulted in the accumulation of thick alluvium and saprolitic valley fill in and beneath the current streams, reaching depths of up to hundreds of meters below the ground surface (borehole logs from the Hawaiʻi Commission on Water Resource Management). As will be shown, since most OSDS in Kāneʻohe are located at shallow depths in this alluvium layer, the hydrogeological characteristics of the valley fill and the positioning of the less permeable dike-bearing basalts that bound it act as primary controls on contaminant transport within the subsurface.

Large quantities of high-elevation groundwater are stored within the Koʻolau rift zone in Kāneʻohe, impounded by low-permeability dikes (Takasaki and Mink, 1985). In the dike-free regions, groundwater is primarily present as a basal freshwater aquifer ("freshwater lens") floating above more dense saltwater. A conceptual cross-section representation of the study region hydrology is provided in **Figure 2**; detailed information on the geologic and hydrologic dynamics in the study area are provided in Section 3.4.

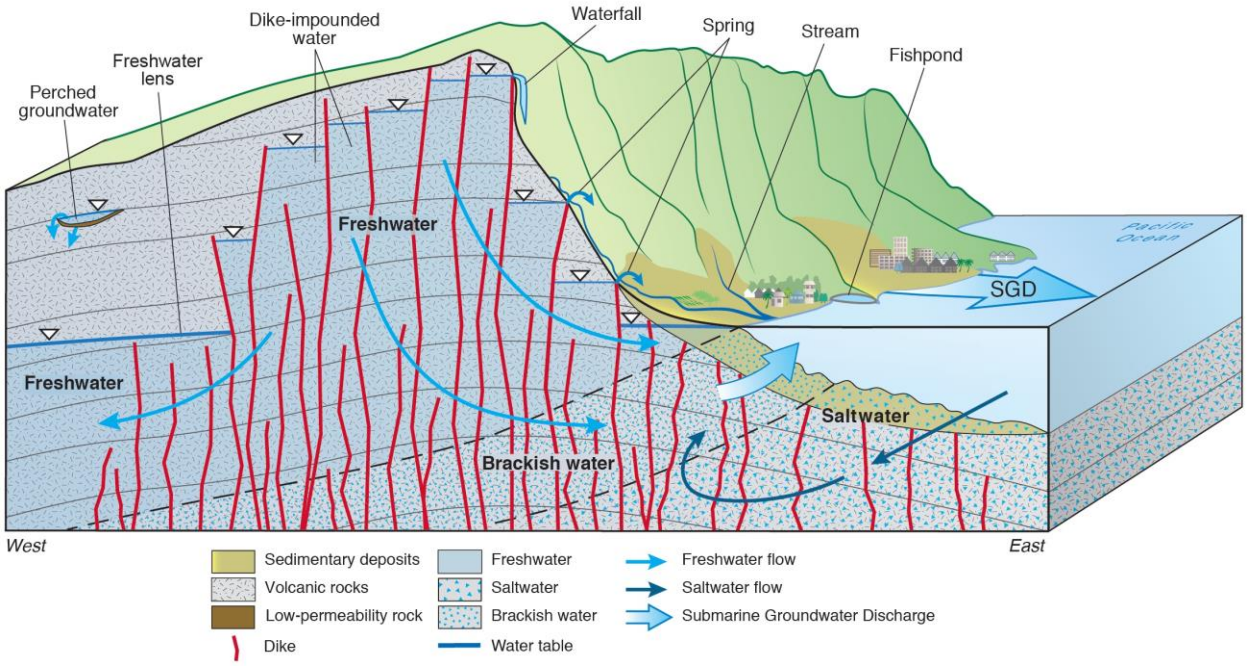

Figure 2: Conceptual model of Kahaluʻu hydrology. Bedrock consists of interbedded lava flows with interspersed vertical volcanic dikes that extend seaward and impede the landward flow of saltwater beneath the freshwater lens. At high elevations where dikes reach the surface, high-level groundwater is stored, which is a significant source of baseflow for most of the major streams in the area. A surficial valley fill sediment (i.e., alluvium, saprolite) layer is present in and around the major streams, reaching depths of up to hundreds of meters.

3.0 METHODS

3.1 Stream gauging and seepage runs

In order to understand hydrologic transport pathways within the study area, stream gauging and stream seepage runs were utilized to evaluate surface flow and delineate stream reaches that are gaining or losing groundwater. Stream gauges were installed at downstream locations in Kahaluʻu and Waiheʻe streams to provide endmember stream discharge data. Each stream gauge consisted of a pressure-transducer (Schlumberger CTD Diver) encased in 1" diameter screened piping (PVC or galvanized metal) to collect autonomous readings of stream level and temperature. Groundwater piezometers were installed at a depth of approximately 1 meter in the water table adjacent to each stream gauge to monitor changes in groundwater level and temperature, and serve as groundwater nutrient endmember sampling points. Groundwater piezometer hardware was identical to that of the stream gauges, consisting of a CTD Diver encased in 1" diameter screened PVC. The piezometers were placed approximately five meters inland from stream banks, within boreholes that were cored manually with a hand auger and backfilled with sand. After installation of each piezometer, standing water within the casing was purged with a peristaltic pump for approximately 15 minutes to remove fines and develop a hydraulic connection with the geologic unit. Once each piezometer was developed, a CTD Diver was placed at the bottom of the casing and anchored to the well cap with wire. CTD Divers in the stream gauges and piezometers were set to record measurements every 15 minutes, and one Schlumberger BaroDiver was deployed for barometric compensations. Top of casing (TOC) elevations for each stream gauge and piezometer set were surveyed with a level transit to allow accurate calculation of head gradients between the stream and water table (gauge locations shown in **Figure 7** of Section 4.2). Each gauge was located downstream of the majority of OSDS located along its respective stream. The Kahaluʻu gauge was located immediately upstream of the flood control lagoon below which stream channelization begins (Figure 1).

Stream discharge measurements were collected at each gauging station with a SonTek FlowTracker Acoustic Doppler Velocimeter to establish a rating curve that relates stream level to volumetric stream discharge rate. The total streamflow at a given location was considered the summation

of flow within 12-15 sections equally spaced throughout the cross-sectional width, for which the midsection discharge equation was applied to calculate volumetric flow (Rehmel, 2007). Instrument-calculated uncertainty ranged from 4.8 to 9.6% for Kahaluʻu Stream, and from 10.9 to 19.3% for Waiheʻe Stream. A quality control measurement was made with the FlowTracker at the active Kahaluʻu USGS gauge, and the difference in measured streamflow between our measurement and the USGS telemetry reading at the time of measurement was 3.5%. Discharge measurements were collected over a wide range of hydrologic conditions to ensure the validity of the rating curve. Rating curves established for Waiheʻe and Kahaluʻu streams are shown in **Figure 3**.

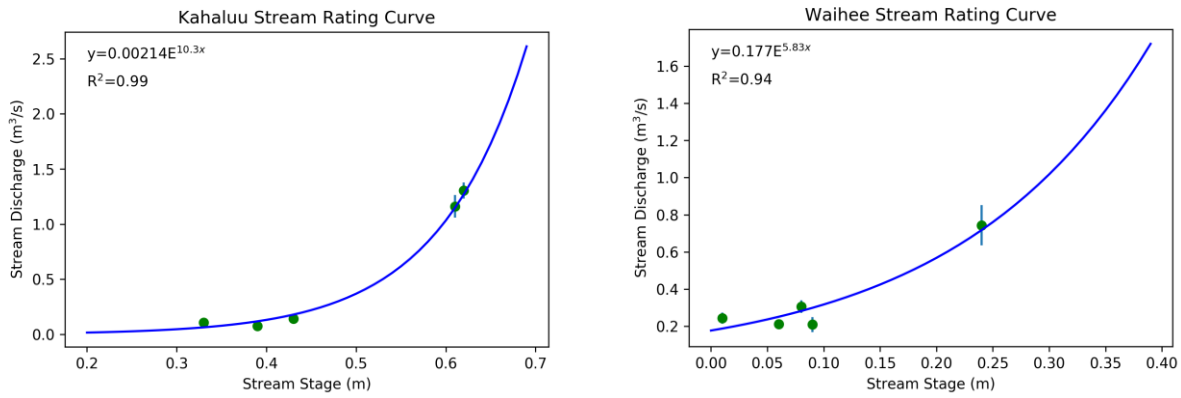

Figure 3: Rating curves for the Kahaluʻu and Waiheʻe downstream gauging stations. Both streams show a strong correlation between stream stage (water height) and stream discharge. All stream discharge measurements were collected with a SonTek FlowTracker Acoustic Doppler Velocimeter.

Seepage runs were conducted in both Waiheʻe and Kahaluʻu streams to delineate “gaining” (gaining water from groundwater) and “losing” (losing water to groundwater) streams reaches (e.g., Donato, 1998; Izuka and Gingerich, 1998; Healy, 2003). A seepage run employs a mass balance approach that consists of dividing a stream into reaches, and then measuring the discharge at the downstream ($Q_{downstream}$) and upstream ($Q_{upstream}$) boundary of each reach. After accounting for all tributaries ($Q_{tributaries}$) and diversions ($Q_{diversions}$) within the reach, the difference between the downstream and upstream discharge rate is the rate at which the stream reach is gaining water (if the value is positive) or losing water (if the value is negative). The mass balance equation is as follows:

$$Q_{downstream} - Q_{upstream} + \Sigma Q_{diversions} - \Sigma Q_{tributaries} = Q_{GW} \quad (1)$$

Our stream gauges acted as the downstream boundaries for the seepage runs, and active USGS gauging stations in Kahaluʻu Stream (USGS Site #16283200) and Waiheʻe Stream (USGS Site #16284200) were used as the upstream boundaries. The length of stream between the downstream and upstream boundaries was split into sections, and the stream discharge rate was measured at the downstream and upstream boundary of each section. Sections were chosen during a preliminary stream walk, with preference given to locations where streambed characteristics were most ideal for stream discharge measurements. Ideal locations were characterized by clearly defined streambed edges, a lack of obstructions in and around the streambed, and water deep enough to allow use of the FlowTracker (depth > 0.10 meters) but shallow enough to wade. Seepage runs for Kahaluʻu and Waiheʻe streams were completed in March 2017 (wet season) and July 2017 (dry season), with the exception of a segment upstream of the USGS Kahaluʻu gauge, which was measured in May 2018.

3.2 Water budget

A preliminary water budget analysis was conducted to evaluate hydrologic sources and sinks for each watershed. Precipitation and evapotranspiration data were obtained from Giambelluca et al. (2013) and recharge and streamflow data records from Engott et al. (2015) and the USGS National Water Information System (2018), respectively. Streamflow for ungauged streams (Ahuimanu, Kaʻalaea, and Haiamoa) was calculated by utilizing multiple regression analysis for streamflow, rainfall, and watershed area data from Kahaluʻu and Waiheʻe streams. Runoff was calculated by subtracting evapotranspiration and recharge from precipitation, and baseflow was calculated by subtracting runoff from streamflow. To validate baseflow calculations, the Base Flow Index (BFI) method (Institute of Hydrology, 1980a, 1980b) was used to calculate baseflow for periods of N=5 days (Barlow et al., 2015). In the streams gauged as part of this study (Kahaluʻu and Waiheʻe, see Section 3.1), USGS stream gauge data was correlated to this study's downstream gauges, and this correlation was applied to historical USGS data for calculation

of streamflow and baseflow. The idea is that the downstream gauges we installed are more representative of endmember stream flow volumes, as the average flows at our downstream gauges are 41% and 55% greater than at the upstream USGS gauges for Kahaluʻu and Waiheʻe streams, respectively. Pumping data was provided by the Hawaiʻi Commission on Water Resources Management. All data utilized for the water budget are for the period of 1978-2007, which is the period of rainfall data (Giambelluca et al., 2013) on which the aforementioned USGS recharge estimates (Engott et al., 2015) are based.

3.3 Thermal infrared imaging

Thermal infrared (TIR) imaging is a useful tool for mapping SGD in regions where a temperature contrast exists between groundwater and ocean water. Since groundwater is insulated from the sun, it does not experience the same temporal and diurnal heat fluxes as surface water. This results in temperature gradients between groundwater inputs and receiving waters (e.g., ocean, streams) that are easily detectable by high-resolution TIR imaging. Within the study area, a significant temperature gradient of 2.5°C exists between groundwater (23.1 ± 2.4° C, n=15, field measured values) and sea surface temperature (25.6 ± 0.8° C, n=16598, NOAA 2018 National Data Buoy Center, Station 51207 - Kāneʻohe Bay), making the study area particularly well suited for TIR imaging of SGD.

TIR imaging involves the digital sensing of infrared radiation via the detection of electromagnetic waves with wavelengths of approximately 3.5 to 20 micrometers. TIR imaging is utilized for a wide variety of applications and the recent rise of unmanned aerial vehicles (UAV, “drones”) has added new capacity for high-resolution imaging and data-collection flexibility. Compared to high-altitude aircraft TIR imaging (A/C-TIR), which has been used to locate groundwater discharge to rivers, lakes, estuaries, and the ocean (Banks et al., 1996; Faux et al., 2001; Duarte et al., 2006; Mulligan and Charette, 2006; Johnson et al., 2008; Danielescu et al., 2009; Handcock et al., 2012; Culbertson et al., 2013; Kelly et al., 2013; Tamborski et al., 2015, Kennedy, 2016; McCaul et al., 2016), unmanned aerial vehicle TIR (UAV-TIR) imaging is a more recent and cost-effective technology that provides higher resolution imagery and offers flexibility for routine monitoring. While use of A/C-TIR and/or satellite thermography is more effective for

large-scale mapping of SGD, UAV-TIR is ideal for investigating local SGD features on a small scale. Recent studies (Kennedy, 2016, Lee et al., 2016) have utilized UAV-TIR to image known locations of point-source SGD, as delineated by A/C-TIR surveys. Our study aims to demonstrate the effective use of UAV-TIR as a reconnaissance and mapping tool for SGD, independent of preliminary A/C-TIR surveys.

3.3.1 UAV-TIR data collection

UAV-TIR flights were conducted following low tide on the mornings of 18 August 2017 (low tide: 05:38 HST, flights: 06:30-08:00 HST) and 19 August 2017 (low tide: 06:27 HST, flights: 06:40-07:35 HST) to map point-source and diffuse SGD along the 6 km stretch of study area coastline. Flights were performed on calm and clear days with no appreciable rainfall. Thermal imagery was collected with a FLIR Tau 2 640 thermal camera and TeAx ThermalCapture hardware, mounted on a DJI Matrice 100 quadcopter powered by a Lithium Polymer (LiPo) battery, allowing for individual flight times of approximately 20 minutes. TIR imagery was collected at a rate of nine frames per second (9 Hz), geo-tagged with spatial coordinates from an onboard GPS unit (Navilock NL-302U USB GPS Receiver), and stored on an onboard USB thumb drive. TIR imagery was relayed to a ground-station viewing screen for real-time analysis, allowing for UAV positioning adjustments as needed. RGB imagery was collected simultaneously with TIR data at a frame rate of 60 frames per second (60 Hz) from a GoPro HERO3+ camera, aiding in feature identification and georeferencing of UAV-TIR data. Flights were conducted as per FAA (2016) guidelines.

In order to ground-truth UAV-TIR data, in situ temperature data was collected from the topmost layer of surface waters from thermistors (HOBO Pendant, Onset Computer Corporation) anchored in the UAV-TIR field of view. The thermistors were mounted to reflective buoys, providing ground control points and temperature calibration points that were easily identifiable in TIR imagery during post-processing. Additional ground control points, consisting of square aluminum sheets approximately 40 cm x 40 cm in dimension, were deployed within the UAV-TIR field of view as necessary.

Each UAV-TIR flight was followed by a shore-parallel temperature/salinity survey to confirm the presence of cold freshwater seeps. These in situ data were collected from approximately 20 meters offshore with a YSI EXO2 multiparameter sonde at a data rate of 1 Hz.

3.3.2 UAV-TIR data processing

Raw imagery was imported and reviewed in ThermoViewer (TeAx Technology) software to ensure adequate scene composition, scaled appropriately for scene temperatures, and then exported as digital number (DN) JPEGs. Images were then corrected for wide-angle lens vignetting (i.e., cooling around the image edges due to signal fall-off), with pixel-by-pixel batch corrections based on a normalized blackbody calibration image of the TIR camera lens. Vignette-corrected JPEG images were then mosaicked in Microsoft ICE, and the resulting mosaics exported as single images. The mosaics were then imported into ESRI ArcMap software, and georeferenced using available ground control points. At least four ground control points were utilized for proper georeferencing of each mosaic. The reflective in situ temperature buoys were utilized as offshore ground control points, and onshore ground control points were provided by known locations of landforms and structures that were visible in the thermal imagery. Ground control points were evenly distributed throughout the mosaic as best as possible to ensure proper spatial alignment, and residual spatial errors (calculated by ArcMap) were kept below 2 meters. Each georeferenced JPEG mosaic was converted to a temperature raster by utilizing the raster math tools in ArcMap to apply the linear relationship between pixel DN range (0-255) and temperature range. TIR temperature values were then corrected to in situ temperature measurements, and a false color scale applied for ease of data interpretation. These post-processing methods (outlined in **Figure 4**) are easily replicable, and significantly increase the potential of UAV-TIR as an independent SGD mapping tool.

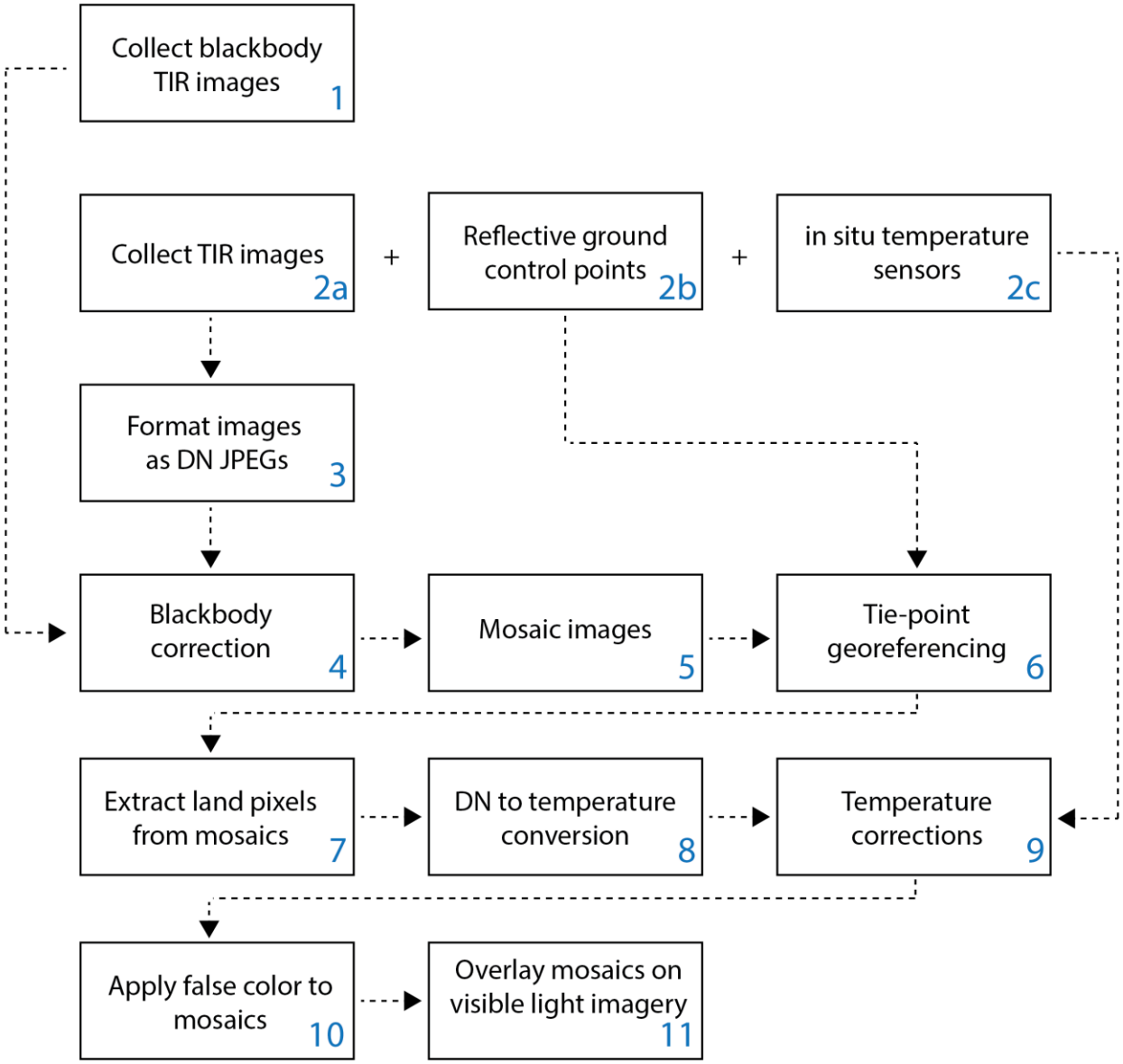

Figure 4: UAV-TIR data collection and post-processing flowchart. Python scripting was utilized for automation of blackbody corrections (step 4), Microsoft Image Composite Editor utilized for image mosaicking (step 5), and ESRI ArcMap utilized for georeferencing, DN to temperature conversion, temperature corrections, false coloring, and data overlays (steps 6-11).

3.4 Numerical groundwater modeling

Numerical hydrologic modeling was used to simulate aquifer conditions for fate and transport analysis of contaminants (in this study, dissolved inorganic nitrogen), and quantification of baseflow and SGD. Groundwater Modeling System (GMS) software was used to run the MODFLOW and MT3DMS codes, providing three-dimensional steady state flow and transient solute-transport modeling capabilities, respectively. The terrestrial model domain is 23 km², modeled as a 140x140 grid of 50 meter cells, encompassing six watersheds (Figure 1): Ahuimanu, Kahaluʻu, Kahaluʻu segment, Waiheʻe, Haiamoa, and Kaʻalaea. The model area is bounded by the Koʻolau ridgeline to the southwest, shore-perpendicular ridgelines to the northwest and southeast, and Kāneʻohe Bay to the northeast. In order to simulate coastal hydrologic dynamics, the model boundaries were extended approximately two kilometers offshore. The model domain is a part of the Koʻolaupoko aquifer, which is recharged primarily by orographic rainfall on the windward slopes of the Koʻolau range. Recharge varies drastically in this region, primarily due to high rainfall variability, which ranges from approximately 1300 mm/yr in the coastal plains to 4600 mm/yr near the Koʻolau ridgeline (Giambelluca et al., 2013). Other factors influencing recharge include surface geology (Sherrod et al., 2007), land use, fog drip, and irrigation. All of these factors are accounted for in the USGS recharge coverage for Oʻahu (Engott et al., 2015), which was utilized as the recharge input for the model.

Although limited subsurface lithological information is available for the study area, its geologic history, surface geology, and topography provide insight into its subsurface hydrogeology. A significant portion of the modeled area along the Koʻolau rift zone contains >50% volcanic dikes, and is thus considered a dike complex (Izuka et al., 2015). Previous studies indicate that these low-permeability sheet-like volcanic dikes reduce the bulk permeability of the surrounding flank lavas (Takasaki and Mink, 1985; Hunt, 1996; Izuka and Gingerich, 1998). Alluvium and weathered basalt saprolite substrate overlies interbedded lava flows in each valley, with fill thickness related to surface topography. Fill thicknesses were estimated for each valley by analyzing valley-transverse topographic cross sections for every 25 meters of elevation gain. For all cross sections, the steep upper slope of each ridge sidewall was extended downwards, and the intersection point of the two slopes was considered to be the depth of

valley fill incision (Rotzoll and El-Kadi, 2007; **Figure 5**). Based on this analysis, depth of valley fill ranges from 0 to 425 meters, and decreases with increasing distance from the shoreline (results shown in **Figure 6**). These depths are consistent with findings and observations from studies in other regions of O‘ahu (Oki, 2005; Rotzoll and El-Kadi, 2007). Based on analysis of borelogs provided by the Hawai‘i Commission on Water Resource Management, it was determined that approximately the top 23% of valley fill deposits consist of fine-grained alluviual siliclastic sediments, and the lower 77% consists of highly weathered bedrock (i.e., saprolite). The model was divided into six layers with each layer consisting of one or more of the following lithologic classifications: unconsolidated fill (alluvium, saprolite, marine sediments, beach sediments) or dike-complex basalt. To increase model efficiency, the bottom of the model was truncated to the bottom of the Ghyben-Herzberg lens or 300 meters below mean sea level – whichever was greatest. When the depth of the Ghyben-Herzberg lens exceeded 2000 meters, the model bottom was truncated at 2000 meters with the assumption that no flow exists at deeper depth due to material overburden. Hydraulic conductivity values were estimated in MODFLOW by calibration utilizing hydraulic head values from 11 observation points (7 wells and 4 springs). Nine of these observation points were located in the valley fill and two in the basalt. Model inputs and data sources are provided in **Table 2**.

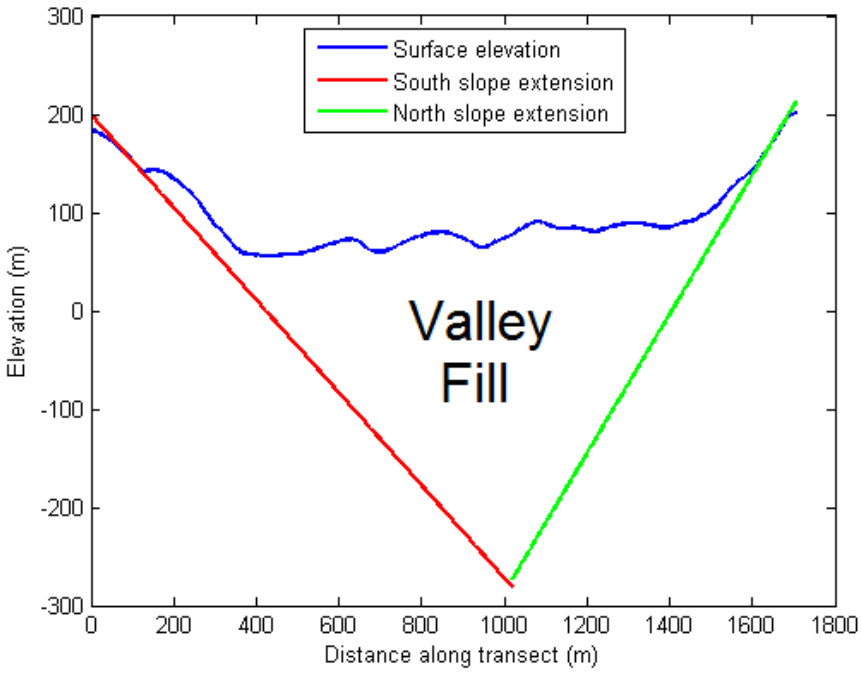

Figure 5: Example valley-transverse topographic cross section, with lines extending the upper slope of each ridge sidewall to an intersection point, which is the estimated depth of valley fill, based on the conceptual geomorphic model from Macdonald et al. (1983).

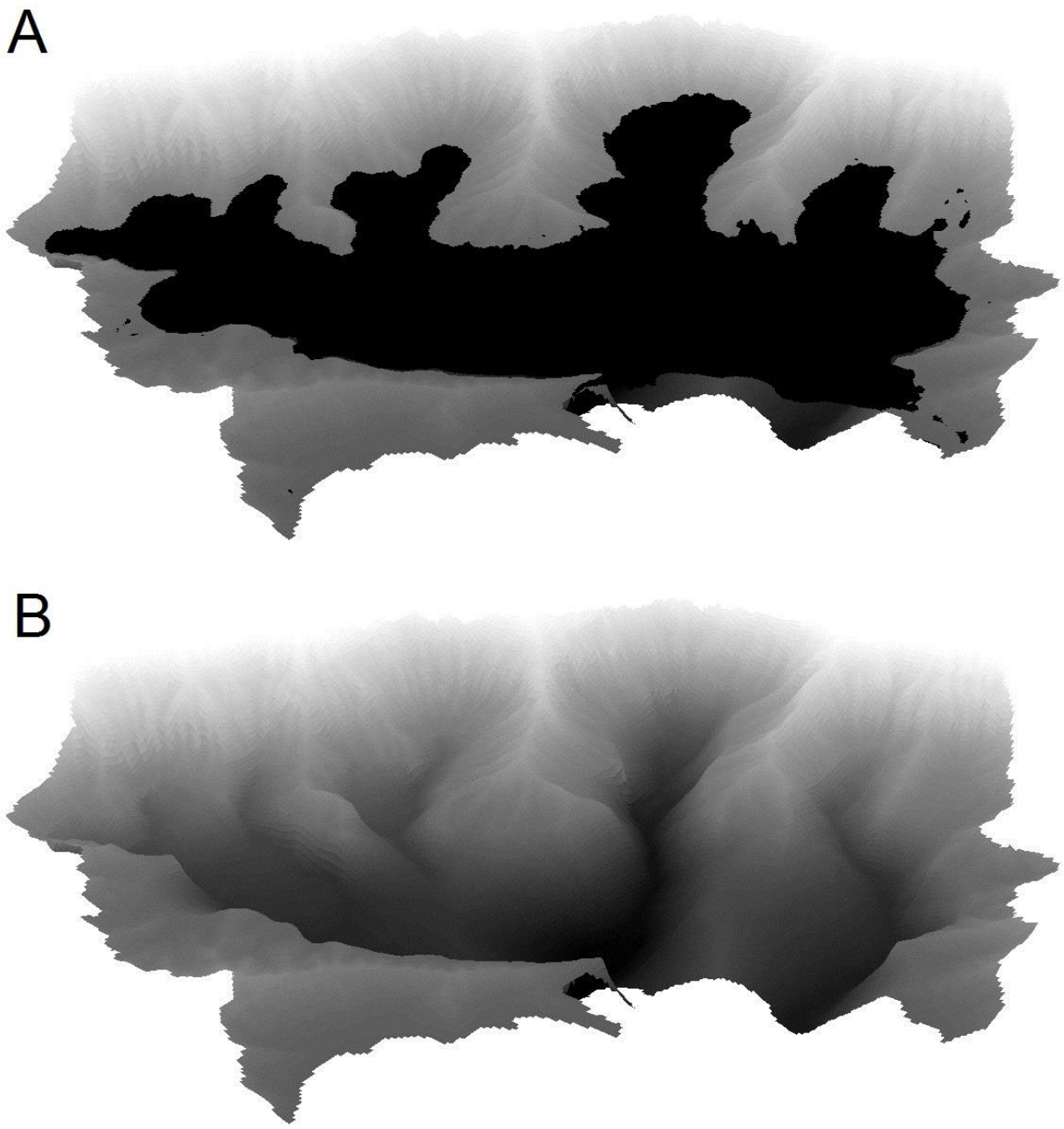

Figure 6: Extrapolated three-dimensional visualization of study area topography with valley fill (A) and without valley fill (B), based on the valley-transverse cross section analysis method. B is taken as the top of basalt. The estimated thickness of valley fill varies from 0 to 425 meters.

Table 2: Model parameters and data sources.

Parameter	Value	Units	Data Source
Elevation / Bathymetry	-17 – 859	m	NOAA (2007) / NOAA (2011)
Recharge	0.04 – 2.43	m/yr	Engott et al. (2015)
GW Pumping	30745	m^3/d	Honolulu Board of Water Supply
OSDS Effluent	2525	m^3/d	Whittier and El-Kadi (2009)
Porosity (Valley Fill)	0.30	-	Mean of measured values (n=26)
Porosity (Dike-Intruded Basalt)	0.05	-	Hunt (1996)
Horizontal Hydraulic Conductivity (Valley Fill)	1.75	m/d	Model calibration (Section 4.4.1)
Horizontal Hydraulic Conductivity (Dike-Intruded Basalt)	0.11	m/d	
Vertical Anisotropy (Valley Fill)	1	-	Isotropy assumption
Vertical Anisotropy (Dike-Intruded Basalt)	5	-	Hunt (1996)
Streambed Conductance	2	$m^2/d/m$	Calibration and sensitivity analysis
Streambed Conductance (channelized)	0.5	$m^2/d/m$	Calibration and sensitivity analysis
Longitudinal Dispersivity	5	m	Guided by Oki (2005)
Bulk Density (Valley Fill)	1100	kg/ m^3	USDA NRCS Soil Survey (2017)
1st Sorption Constant	8×10^{-9}	m^3/mg	Manual calibration with measured values
Rate constants (dissolved and sorbed)	5×10^{-4}	1/d	

DIN was chosen as the OSDS contaminant for the MT3DMS model, but the transport of DIN in the subsurface can also be considered a proxy for other OSDS contaminants. OSDS inputs were simulated via a 100-meter recharge grid into the top layer of the model, with each grid cell input consisting of the sum of OSDS effluent and the average OSDS effluent concentration within the cell area. The total OSDS input into each grid cell was calculated with OSDS location, type, and estimated effluent quantities and concentrations documented by Whittier and El-Kadi (2009). A total of 12 groundwater sample points, consisting of our well, tunnel, and coastal piezometer sample locations, were utilized as observation points for model validation. Concentrations from two coastal piezometer locations where salinity exceeded 1 psu were corrected for salinity with the following formula:

$$c_{fresh} = \frac{c_{sample} - c_{marine} f_{marine}}{f_{fresh}} \quad (2)$$

where *c* represents concentration and *f* represents the fraction of each endmember (fresh and saline) present in the sample. This method, which assumes conservative mixing in the subterranean estuary (STE), was chosen due to a lack of data to qualify removal rates in the STE. Fresh and marine

endmember salinities utilized were 0.07 and 34.37 psu, respectively, based on samples collected from drinking water wells (fresh) and offshore (marine) samples collected as part of this study and further discussed in Section 3.5 and Section 4.3. Bulk density was set as 1.10 kg/m^3 based on a weighted average of the soils in the study area, as delineated by the USDA NRCS Soil Survey (2017). MT3DMS chemical reaction parameters (1st sorption constant and rate constants; see Table 2) were manually varied to achieve a reasonable fit of modeled OSDS DIN with measured DIN values. In instances where groundwater sample points fell within 20 m of a cell boundary, the average concentration of the bounding cells was utilized.

3.5 Geochemical analyses

A total of 166 water samples (including 12 duplicate samples) were collected throughout the study area, and analyzed for concentrations of dissolved inorganic nutrients (data in **Appendix D**). Endmembers were obtained for dike-impounded groundwater, basal groundwater, stream headwaters, stream outflows, and ocean water. All sample locations were surveyed with a YSI EXO2 multiparameter sonde for measurement of temperature, salinity, pH, total dissolved solids (TDS), and dissolved oxygen (data in **Appendix C**). Nutrient analyses were performed by the Hawai‘i State Department of Health Analytical Laboratory and the University of Hawai‘i SOEST Laboratory for Analytical Biogeochemistry, with both facilities utilizing a Seal Analytical AutoAnalyzer III. In addition to baseline samples collected for watershed-scale analysis of DIN sources and sinks, samples were collected from seepage run segments, stream gauge and piezometer stations at various flow conditions, and stream and coastal locations where groundwater seepage was evidenced by low temperature, low salinity, or visible bubbling and/or iron precipitation at the surface.

Eight DIN samples were collected from groundwater wells to act as validation for MT3DMS model outputs. Low-elevation groundwater sample points were relatively limited throughout the study area, as most drinking water is sourced from high-elevation groundwater tunnels that breach the high-elevation dike-impounded groundwater. Of the 31 private wells in the study area, most were installed in the mid-20th century and have since been abandoned or capped. Three private wells were successfully accessed and

sampled, in addition to three high-elevation municipal tunnels and wells, and six low-elevation groundwater piezometers.

Ocean DIN samples were collected at all locations delineated by UAV-TIR as potential SGD seeps. These samples were collected within the center of the seep area delineated by UAV-TIR. Baseline DIN samples were collected from adjacent, non-impacted watersheds, and from offshore (300-500 meters) locations within the study area. An effort was made to ensure that baseline samples were collected from locations with salinity greater than 34 psu.

Total N, Total P, nitrite+nitrate (NO_2^-+NO_3^{2-}), and ammonia+ammonium (NH_3+NH_4^+) were run as separate analyses. Dissolved inorganic nitrogen (DIN) was computed as the sum of nitrate+nitrite and ammonia+ammonium. Dissolved organic nitrogen (DON) was considered to be the remainder of Total Nitrogen after subtracting the quantity of DIN. In instances when Total Nitrogen was not analyzed, DON was not calculated.

4.0 RESULTS

4.1 Stream gauging and seepage runs

Our seepage runs for Waiheʻe and Kahaluʻu streams (streamflow data in **Appendix B**) found that during baseflow conditions, streamflow varied by no more than 7% between upstream USGS gauges and the downstream gauges installed for this study. However, small influxes and outfluxes of water from/to groundwater were found to occur in various stream reaches. These “gaining” and “losing” reaches varied by season for many of the stream reaches, but one particular stream reach of Waiheʻe stream, illustrated in **Figure 7**, was found to be gaining significant quantities of groundwater (25 and 24 m^3/d per meter of stream length, for the wet and dry season seepage runs, respectively). This Waiheʻe stream segment is 137 meters in length, and 27 OSDS units are located with 200 meters of the reach. The most significant gaining section of stream is immediately upstream of the USGS gauge in Kahaluʻu Stream. This section of stream is approximately 698 m long and varies in elevation from 43 to 75 m above sea level, gaining approximately 8 m^3/d of groundwater per meter of stream length. The groundwater gains in this segment account for 47-71% of the total streamflow inputs, and 101 OSDS units are located within 200 meters of this gaining stream reach.

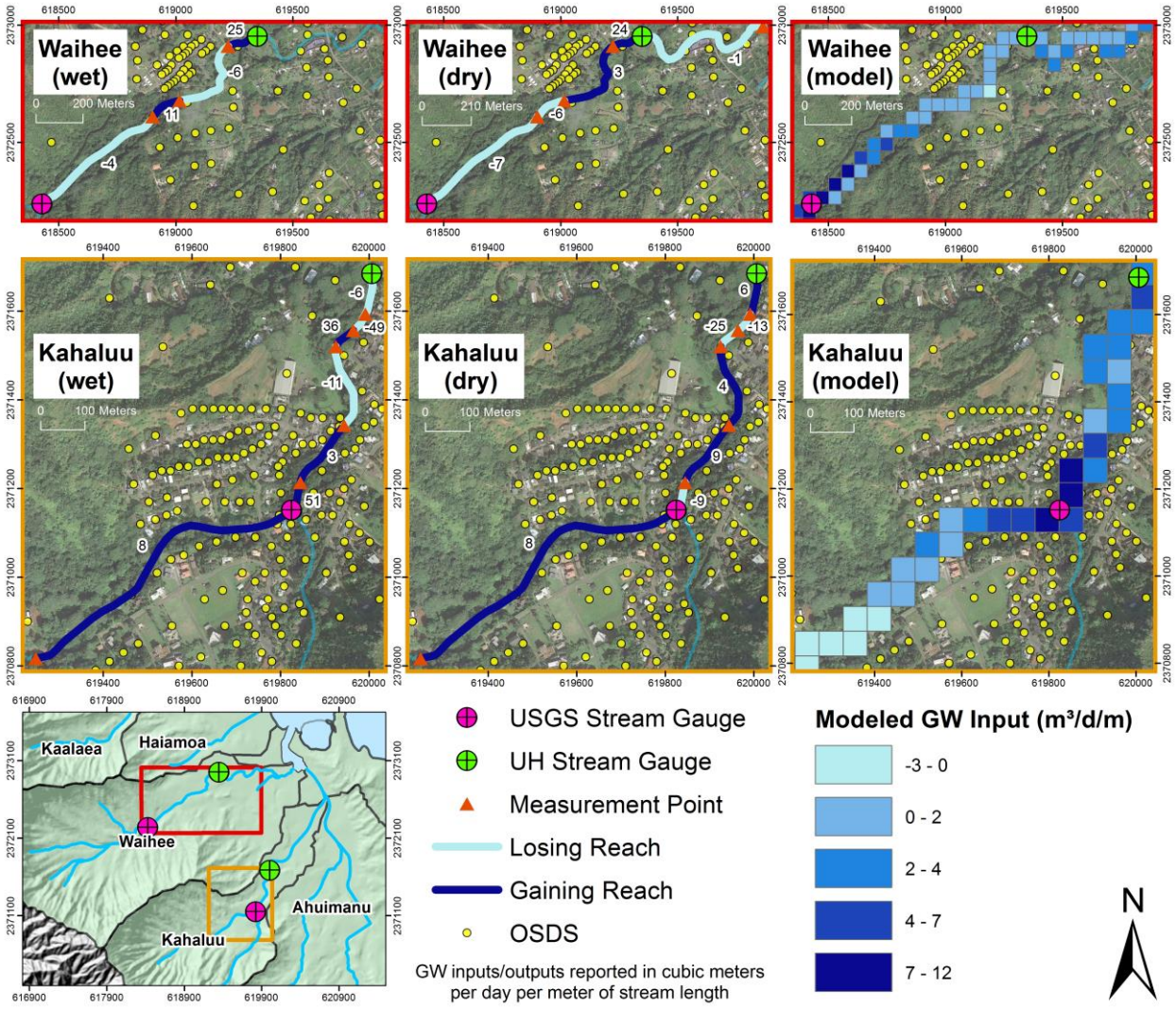

Figure 7: Measured groundwater inputs from seepage runs for Kahaluʻu and Waiheʻe streams during wet season (left panels) and dry season (center panels) conditions, and model-predicted groundwater inputs (right panels). Estimated groundwater inputs are presented in units of cubic meters per day per meter of stream length, with positive numbers signifying a streamflow gain from groundwater and negative numbers signifying a streamflow loss to groundwater. Wet season seepage runs were conducted in March 2017, and dry season seepage runs in July 2017. Model-predicted groundwater inputs to streams represent average values based on model input data from 1978 to 2007 (see Section 3.4). Model resolution is 50 meters.

No significant correlations were found to exist between nutrient concentrations and stream gains or losses. However, based on samples collected under the varying conditions of rating curve measurements at Kahaluʻu Stream, significant correlations were found to exist between stream discharge rate and nutrient concentrations (**Figure 8**). Nutrient data collected during varied flow conditions (0.08 to 1.31 m^3/s) in Kahaluʻu Stream shows strong positive correlations between streamflow and total phosphorus (R^2=0.87) and total nitrogen (R^2=0.85). Most of the increased nitrogen load during high flow events is likely due to an increase in organics, as DON correlates strongly (R^2=0.84) with streamflow, whereas DIN shows a weak negative correlation (R^2=-0.25). Some of this organic load could be sourced from OSDS overflow, as ammonia+ammonium also shows a moderate correlation (R^2=0.53) with streamflow. Dissolved silica, a hydrolysis-weathering product of basalt that is elevated in groundwater (Visher and Mink, 1964), is inversely correlated with streamflow (R^2=-0.91), likely due to dilution of baseflow during high-flow events. These results are similar to correlations noted by Hoover (2002) for Heʻeia and Kāneʻohe streams, which are located directly south of our study area and within the greater Kāneʻohe Bay watershed.

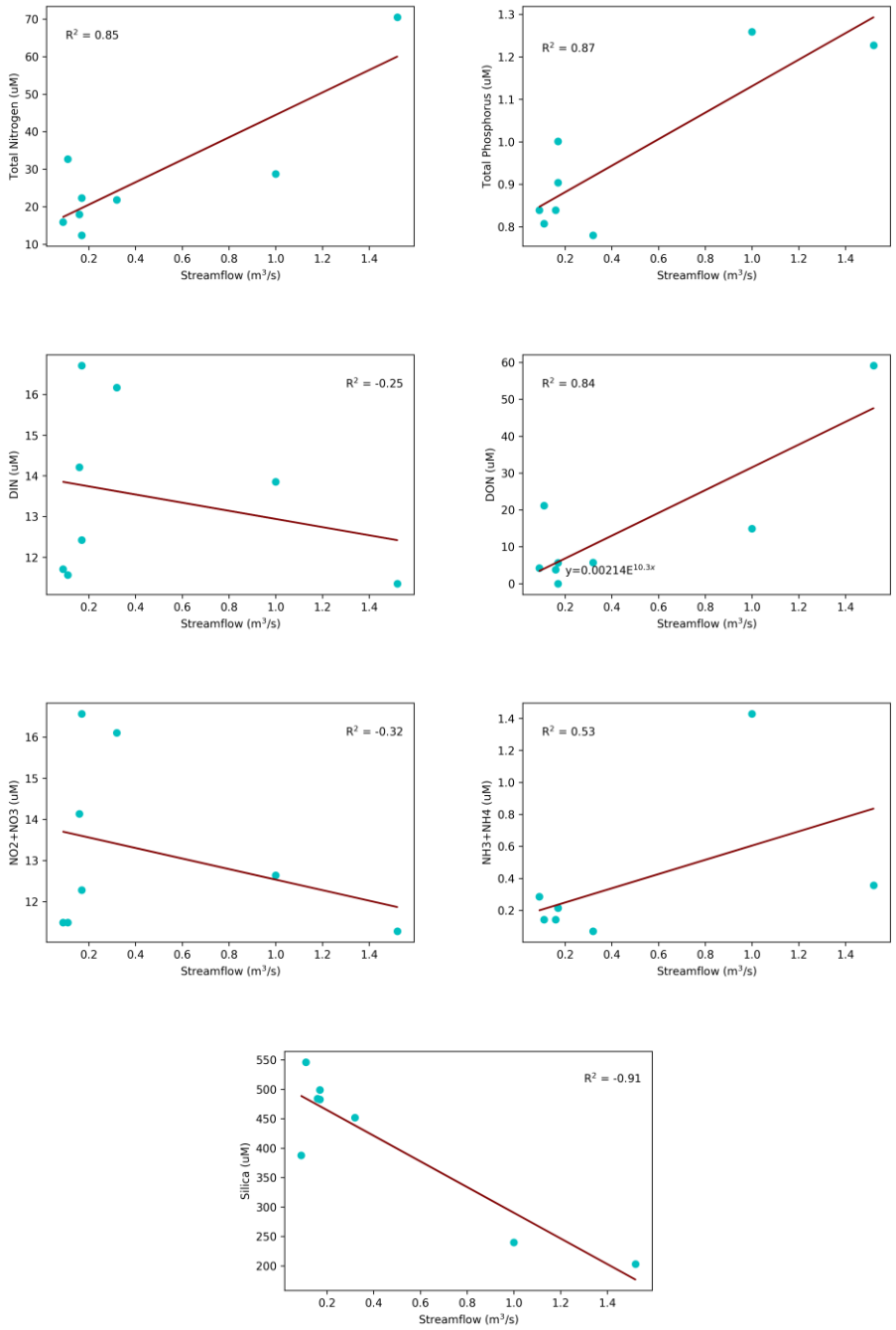

Figure 8: Plots showing correlations between nutrient concentrations and streamflow. All samples (n=8) were collected from Kahaluʻu Stream at the stream gauge location (see UH Stream Gauge - Kahaluʻu location in Figure 7) during varying flow events from October 2016 to April 2018. Strong positive correlations exist between total nitrogen (R^2=0.85), total phosphorus (R^2=0.87), DON (R^2=0.84) and streamflow. A moderate correlation (R^2=0.53) also exists between ammonia+ammonium and streamflow. A strong negative correlation exists between silica (R^2=-0.91) and streamflow.

4.2 Water budget calculations

Water budget calculations for the study area reveal an excess of outputs to inputs, as the sum of recharge, runoff, and evapotranspiration exceeds precipitation. This is evidenced by the negative leakage values presented in **Table 3** and discussed in Section 5.1. Baseflow calculations from the water budget (streamflow minus runoff) and from the Baseflow Index (BFI) method (N=5 days) differed by 20 and 29% for Kahaluʻu and Waiheʻe streams, respectively, showing that baseflow is responsible for approximately 59-81% of the streamflow in the study area. This is comparable to estimations by Hoover (2002) for Heʻeia and Kāneʻohe streams, which are located directly south of our study area and within the greater Kāneʻohe Bay watershed. Baseflow plots from the BFI method are shown in **Figure 9** for the two streams (Kahaluʻu and Waiheʻe) with permanent gauging stations and historic streamflow data.

With a balanced water budget, leakage (i.e., flow out of the aquifer), which in Hawaiian aquifers occurs primarily in the form of submarine groundwater discharge, is considered the remainder of recharge after subtracting pumping and baseflow. As evidenced by the negative leakage values, this water budget does not balance properly, and a possible explanation, first proposed by Takasaki and Mink (1985), is that the high degree of valley incision on the windward side of the Koʻolau range results in a subsurface groundwater divide that lies leeward of the surficial watershed divide (see aquifer delineations in Hunt, 1996). This idea is discussed further in Section 4.4 and Section 5.1.

Table 3: Water budget calculations with data from the period of 1978-2007. Precipitation and evapotranspiration data were obtained from Giambelluca et al. (2013), recharge data from Engott et al. (2015), and pumping data from the Honolulu Board of Water Supply. Streamflow estimates were obtained from the USGS National Water Information System (2018) and corrected to our downstream gauges to account for down-gradient runoff and baseflow contributions. Baseflow was calculated by subtracting runoff from streamflow, and leakage was considered the remainder of recharge after subtracting pumping and baseflow. As evidenced by the negative leakage values, this water budget does not balance properly, and a possible explanation, first proposed by Takasaki and Mink (1985), is provided in Section 5.1.

		INPUTS	**OUTPUTS**					
Wshed	**Area (km^2)**	**Precip. (m^3/yr)**	**ET (m^3/yr)**	**Stream flow (m^3/yr)**	**Rchg. (m^3/yr)**	**Pumping (m^3/yr)**	**Base flow (m^3/yr)**	**Leakage (m^3/yr)**
Ahuimanu	6.25	1.23E+07	6.81E+06	8.51E+06	2.99E+06	2.07E+04	6.02E+06	-3.05E+06
Kahaluʻu	3.38	8.49E+06	3.78E+06	4.09E+06	3.08E+06	3.51E+06	2.45E+06	-2.89E+06
Kah. seg.	1.82	2.69E+06	1.93E+06	0.00E+00	4.34E+05	0.00E+00	0.00E+00	4.34E+05
Waiheʻe	5.86	1.53E+07	6.78E+06	8.84E+06	5.29E+06	7.69E+06	5.57E+06	-7.97E+06
Haiamoa	1.66	3.26E+06	2.01E+06	9.90E+05	7.79E+05	0.00E+00	5.16E+05	2.62E+05
Kaʻalaea	4.56	1.09E+07	5.28E+06	2.52E+06	3.33E+06	0.00E+00	2.62E+05	3.07E+06
TOTAL	**23.52**	**5.29E+07**	**2.66E+07**	**2.49E+07**	**1.59E+07**	**1.12E+07**	**1.48E+07**	**-1.01E+07**

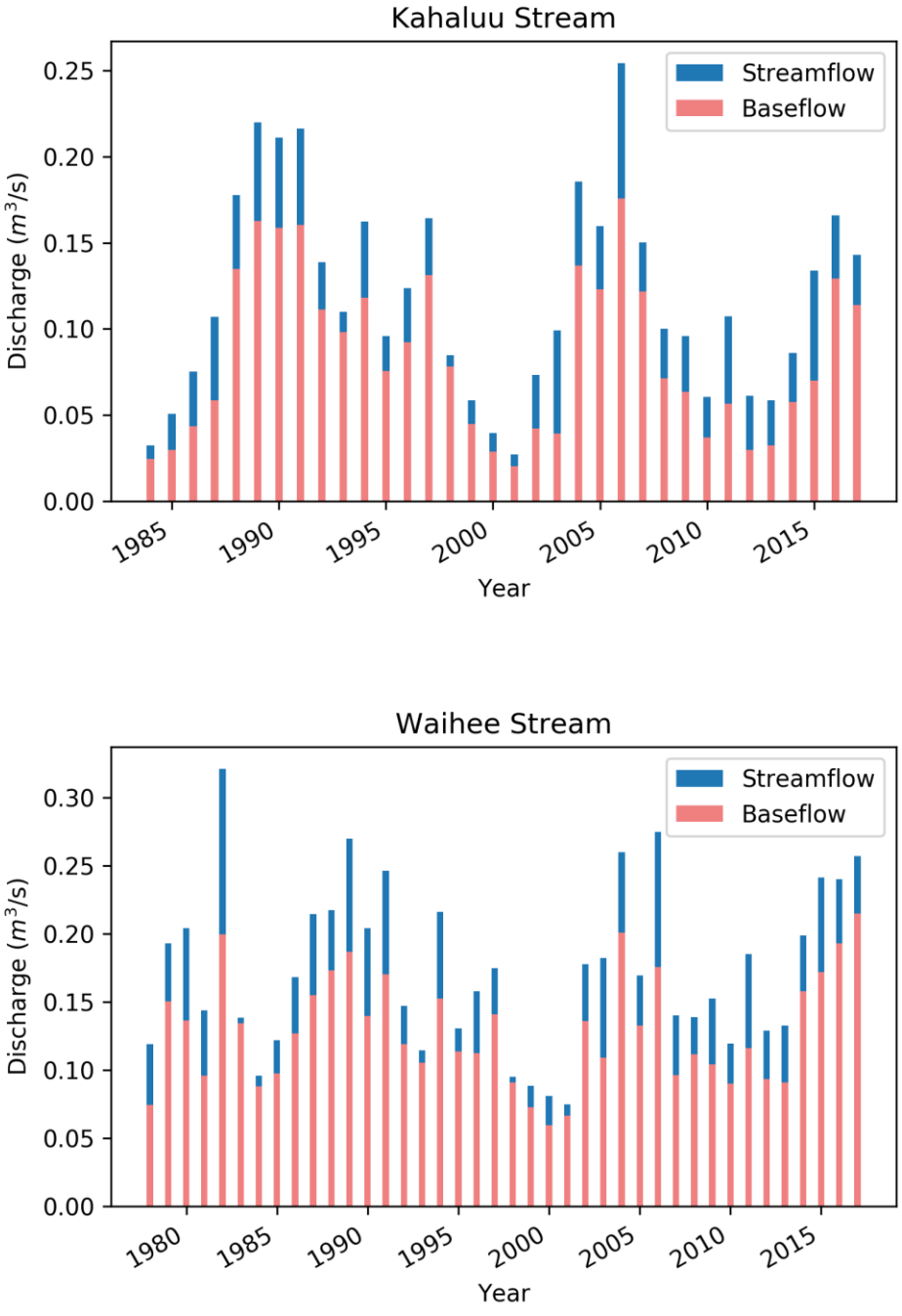

Figure 9: Baseflow and streamflow plots for periods of record from the two permanently gauged streams in the study area -- Kahaluʻu and Waiheʻe – the flows of which are sustained primarily by baseflow. Baseflow was calculated with the Baseflow Index (BFI) method (Institute of Hydrology, 1980a, 1980b) for periods of N=5 days (Barlow et al., 2015).

4.3 Thermal infrared imaging

UAV-TIR imaging and subsequent salinity surveys revealed eight potential submarine groundwater discharge seeps, as shown in **Figure 10**. Stream outflows, thermal inertia differences between coastal settings, and other factors cause regional temperature variations of up to 6 degrees centigrade throughout the study area. Thus, relative temperature differences in localized TIR maps (**Appendix A**), with appropriate temperature scales for each setting, were utilized to delineate seep locations. Each of these locations was sampled for dissolved nutrient, and compared to baseline concentrations, revealing significantly elevated concentrations of silica, total phosphorus (TP), total nitrogen (TN), DIN, NO_2^-+NO_3^{2-}, and NH_3+NH_4^+ in SGD locations (**Figure 11**).

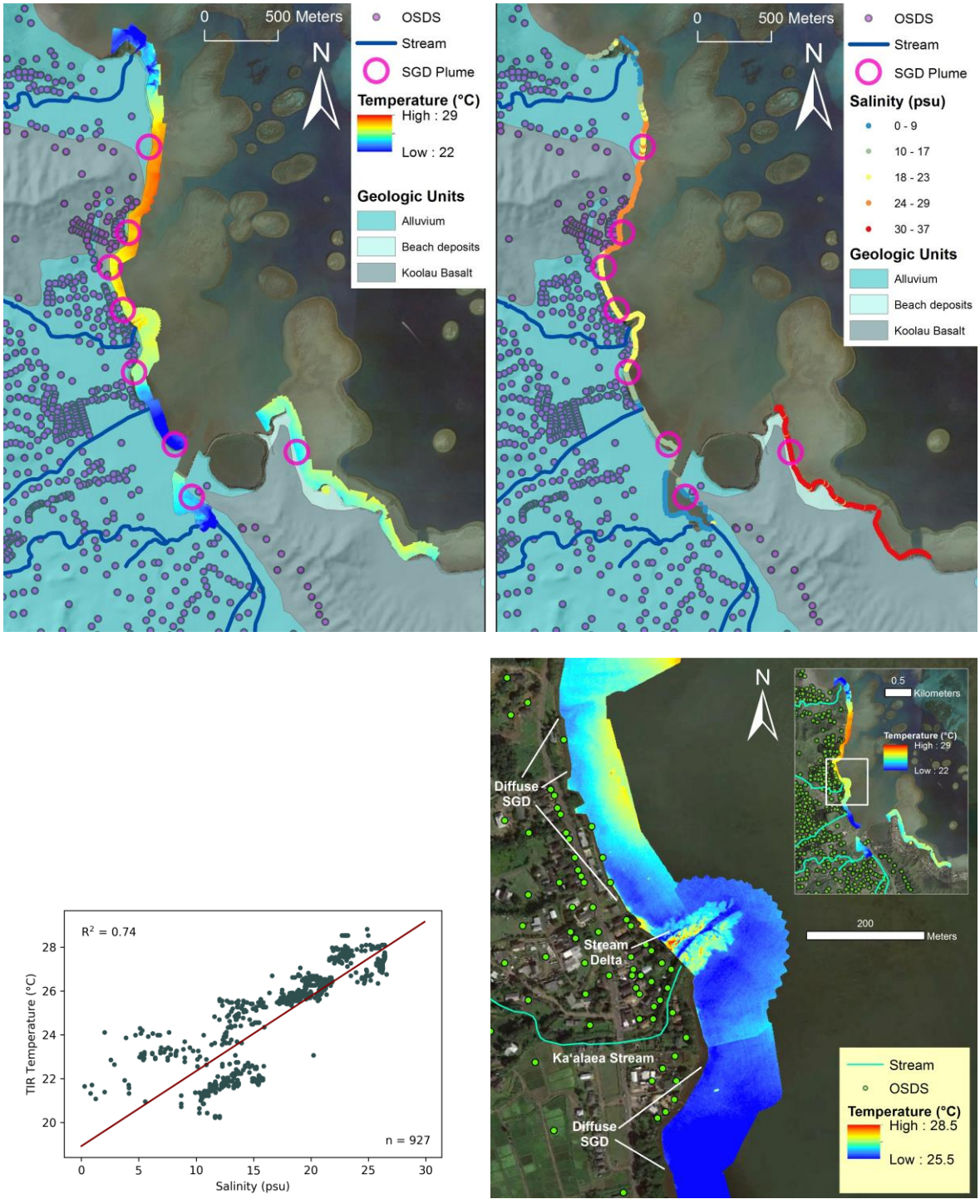

Figure 10: Map of UAV-TIR temperature data (top left) and in situ salinity data (top right), with OSDS locations shown as purple dots. UAV-TIR data were collected during low-tide flights on the mornings of 18 August 2017 and 19 August 2017. Salinity data were collected in situ with a YSI EXO2 multiparameter sonde immediately following UAV-TIR flights. Relationship between TIR temperature and salinity (bottom left) shows a strong correlation. An example localized TIR map from the study area (bottom right) shows diffuse SGD seepage. Localized TIR maps for the entire study area are provided in Appendix A.

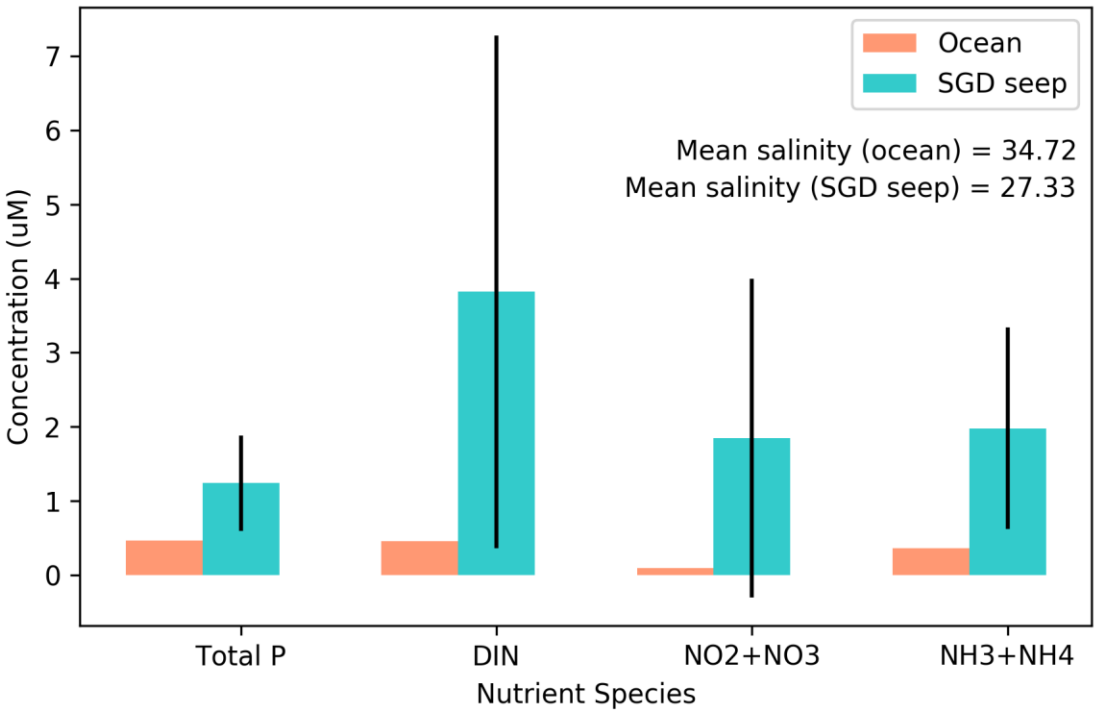

Figure 11: Results of ocean sampling for baseline samples (orange) and SGD seep samples (blue). SGD seeps show consistently elevated concentrations above baseline for all nutrients analyzed: TP, DIN, nitrite+nitrate (NO_2^-+NO_3^{2-}), and ammonia+ammonium (NH_3+NH_4^+). Silica (not shown due to scale), a conservative tracer of groundwater for Hawaiian aquifers, is also elevated in seep samples (mean = 67 μM) relative to ocean (mean = 9 μM). Error bars (one standard deviation) are shown in black.

All of these coastal locations are in or near unconsolidated (alluvium or beach sand) coastal deposits, which suggests that the alluvial deposits may be acting as a direct conduit between OSDS (87% of which are located in shallow alluvium) and the coast. Seven seeps occur through coastal alluvium deposits, and one seep occurs through coastal beach deposits.

Figure 12 shows TIR imagery and a shore-parallel transect plot of TIR temperature in the estuarine confluence of Kahalu‘u, Waihe‘e, and Ahuimanu streams (referred to as the ‘Kahalu‘u estuary’). At a distance of approximately 160 meters along the transect, the temperature abruptly drops from 23.9°C to 23.6°C, and then remains at this temperature until approximately 205 meters along the transect. The lowered temperature values are not likely due solely to the influence of Waihe‘e and Kahalu‘u streams, as temperature increases seaward before decreasing again along the transect -- there is thus likely a local source of groundwater input. As shown, five nutrient samples collected along the transect reveal

increases in nutrient concentrations within the suspected SGD seep. Approximately 20 meters inland from this seep is a septic tank with extremely high effluent concentrations of TN (5712 μM) and NH_3+NH_4^+ (5088 μM). The influence of the septic system is evident in a nearby groundwater piezometer, as DIN (297 μM) and NH_3+NH_4^+ (296 μM) in the piezometer are higher than in any other groundwater, ocean, or surface water sample collected as part of this study. Additionally, TN and TP concentrations are greatest at surface sample location 4, which is in the immediate offshore vicinity of the septic system. Pump tests at the two groundwater piezometers shown in Figure 12 revealed unique results for each location, despite the short distance (20 m) separating the two locations. Each piezometer was installed at a depth of 4 meters below the ground surface, with the water table located approximately 1 meter below the surface. The 1" diameter piezometers were pumped at a rate of 0.75 liters per minute for three minutes, and drawdowns of 0 cm and 29 cm were observed in piezometers 1 and 2, respectively. This result reflects the heterogeneous nature of the subsurface in the study area, and suggests that piezometer 1 has a strong hydraulic connection to the estuary and the groundwater to which the septic tank discharges. This conclusion is also reflected in the groundwater nutrient concentrations, as concentrations of Total N and NH_3+NH_4^{+O2} are significantly higher in piezometer 1 than in piezometer 2 (see Figure 12). This process of utilizing in situ data to confirm that UAV-TIR delineated SGD seeps were hydraulically independent of stream plumes was used for each of the eight delineated SGD seeps, confirming that the freshwater inputs are from groundwater rather than stream inputs.

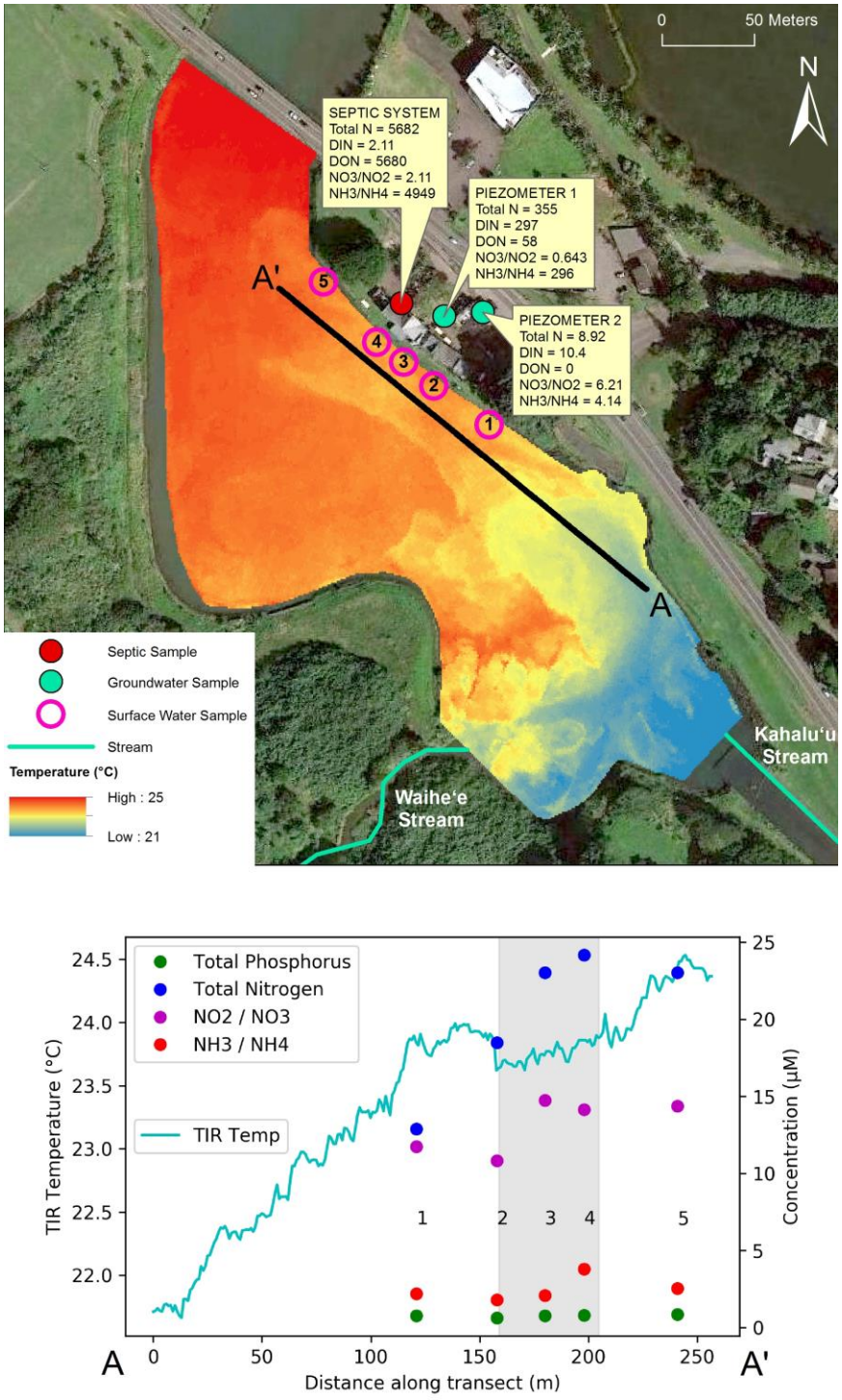

Figure 12: TIR imagery of Kahaluʻu estuary (top) delineating a groundwater seep location and a TIR temperature transect across the seep area, from the stream outlet (A) towards the ocean (A'). The plot (bottom) shows temperature variations and nutrient concentrations for five sample points along the transect. Nutrient concentrations are highest where temperature is lowest and the suspected groundwater contributions are greatest (gray area of plot). TN and NH_3+NH_4^+ concentrations are highest at sample point 4, which is immediately adjacent to a septic tank approximately 20 meters inland.

4.4 Numerical groundwater modeling

4.4.1 MODFLOW outputs

After initial model runs, model-calculated pumping and baseflow were significantly lower (48% and 30% for Kahaluʻu and Waiheʻe streams, respectively) than the known measured values. This further supports the strong possibility that the Koʻolaupoko aquifer boundary does indeed lie leeward of the Koʻolau Crest, as hypothesized by Takasaki and Mink (1985) and Hunt (1996). To account for leeward groundwater influx, a specified flux boundary was applied along the Koʻolau ridgeline, and the flux value adjusted to obtain a reasonable match between modeled and measured baseflow and pumping. Since Waiheʻe valley is the most deeply incised valley in the study area, covers approximately half of the linear distance of the Koʻolau ridgeline in the study area, and is adjacent to the leeward location delineated by Hunt (1996) as having the greatest contribution to the windward Koʻolaupoko aquifer, 70% of the flux was applied to the Waiheʻe watershed. The remainder of the flux was applied to Kahaluʻu (15%), Ahuimanu (10%), and Kaʻalaea (5%) based on valley incision and linear distance along the Koʻolau ridgeline. After accounting for this influx, modeled baseflow volumes were 86% and 69% of the measured 30 year average (1978-2007) baseflow fluxes for Kahaluʻu and Waiheʻe streams, respectively. Model calibration resulted in a strong fit (R^2=0.99) between computed and observed hydraulic head values (**Figure 13**), with no observation points varying by more than 7 m. Calibrated horizontal hydraulic conductivity values are 1.75 and 0.11 m/d for valley fill and dike-intruded basalt, respectively. Average hydraulic head is 61 meters, and the maximum head is 459 m. Model-predicted fresh submarine groundwater discharge (excluding re-circulated saline ocean water) is 1.12×10^7 m^3/yr, which is approximately 45% of the magnitude of stream discharge to the coast, and well within the range of Dulai et al.'s (2016) SGD estimates.

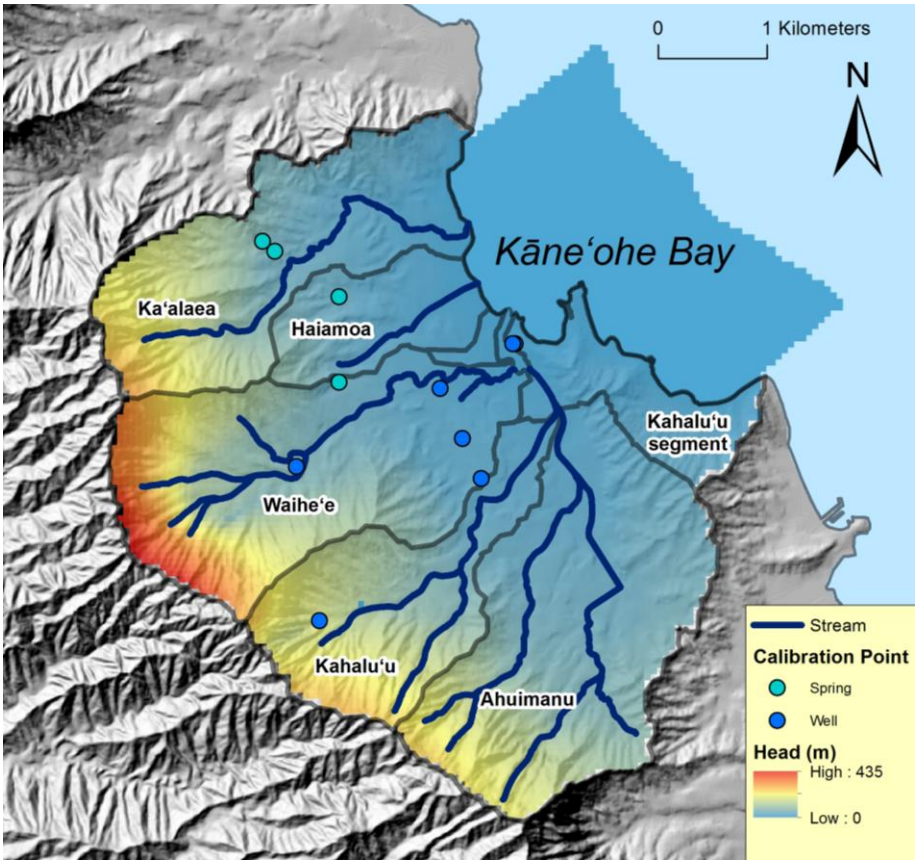

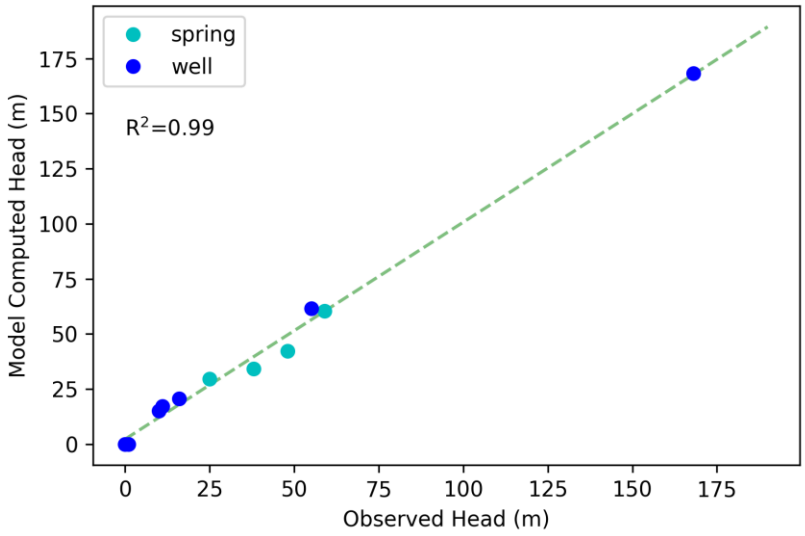

Figure 13: Model computed head values plotted against observed head values for eleven observation points (seven wells, four springs). Observed head values for wells were obtained from well installation bore logs or measured with a pressure transducer as a part of this study. Observed head values for springs were considered to be the elevation of the water surface of the spring.

4.4.2 Sensitivity analysis

Since the vertical anisotropy ratio (ratio of horizontal hydraulic conductivity to vertical hydraulic conductivity) is difficult to estimate or measure for the highly heterogeneous subsurface geology of the study area, sensitivity analysis was conducted to evaluate the effect of vertical anisotropy on model calibration fit and predicted head values. When varying hydraulic conductance for valley fill (between 1 and 5) and dike-intruded basalt (between 0.2 and 5), the coefficient of determination for the observed and computed heads did not drop below 0.99, and average, minimum, and maximum head values did not differ by more than 7 m, 0 m, and 7 m, respectively.

4.4.3 MT3DMS outputs

Due to the relatively slow movement of groundwater in the subsurface, it takes approximately 30 years for OSDS-derived groundwater nutrient concentrations in MT3DMS to reach steady state. However, most of the contaminant mass present at the 30 year steady state is present at 10 years. Based on this finding and the fact that most OSDS in the study area were installed in the past fifty years, groundwater concentrations of OSDS contaminants should be expected to remain steady if no wastewater infrastructure changes are made. Contaminant transport results show the highest concentrations of DIN in Layer 1, which spans from ground surface elevation to 5 meters below msl, where most OSDS are present. Concentrations consistently decline with depth, and no appreciable OSDS DIN is present below a depth of 30 meters below msl.

Modeled and measured DIN concentrations are presented in **Table 4**, and the spatial distribution of shallow groundwater (>-5 m above msl) DIN, as computed via MT3DMS contaminant transport simulation, is presented in **Figure 14**. According to the model, steady state OSDS DIN concentrations are highest in the Haiamoa watershed, and second highest in the Kahaluʻu watershed. In both of these watersheds, OSDS impacts extend to the upstream boundaries (Haiamoa) or nearly to the upstream boundaries (Kahaluʻu). The maximum modeled OSDS DIN concentration is 2.48 mg/L (177 μM), which is below the 10 mg/L threshold set by the EPA (U.S. EPA, 2009). However, since chemical transport parameters were manually adjusted to match measured concentrations, modeled concentrations may greatly differ from measured values, particularly in areas where measured data is limited. Additionally,

total DIN concentrations could exceed 10 mg/L if OSDS DIN is coupled with DIN from other sources, such as agriculture (Whittier and El-Kadi, 2009).

Table 4: Modeled OSDS DIN and measured DIN concentrations for all groundwater samples. Field-measured values include all sources of DIN, whereas modeled DIN includes only DIN from OSDS inputs.

No.	Type	Substrate	Modeled OSDS DIN (mg/L, μM)	Measured DIN (mg/L, μM)
1	Tunnel	Dike-Intruded Basalt	0.00 (0.0)	0.20 (14.3)
2	Well	Dike-Intruded Basalt	0.00 (0.0)	0.12 (8.6)
3	Well	Dike-Intruded Basalt	0.00 (0.0)	0.16 (11.4)
4	Well	Dike-Intruded Basalt	0.06 (4.3)	0.04 (2.9)
5	Well	Dike-Intruded Basalt	0.04 (2.9)	0.08 (5.7)
6	Well	Saprolite	0.34 (24.3)	0.14 (10.0)
7	Piezometer	Alluvium	0.15 (10.7)	0.25 (17.8)
8	Piezometer	Alluvium	0.17 (12.1)	0.11 (7.9)
9	Piezometer	Alluvium	0.01 (0.7)	0.15 (10.7)
10	Piezometer	Alluvium	0.87 (62.1)	0.80 (57.1)
11	Piezometer	Alluvium	0.35 (25.0)	0.62 (44.3)
12	Piezometer	Alluvium	0.00 (0.0)	0.48 (34.3)
		AVERAGE	**0.17 (12.1)**	**0.26 (18.6)**

Samples 1-3 were collected from domestic supply wells and tunnels up-gradient of OSDS impacts. Samples 4-6 were collected from private wells, samples 7 and 8 were collected from our near-stream piezometers discussed in Section 3.1, and samples 9-12 were collected from coastal piezometers. The relationship between modeled OSDS DIN and measured DIN concentrations is provided in Figure 14. Sample 12 is an outlier that suggests the presence of a significant localized non-OSDS nitrogen source. When excluding sample 12 from analysis, the coefficient of determination (R^2) in Figure 14 increases from 0.55 to 0.73.

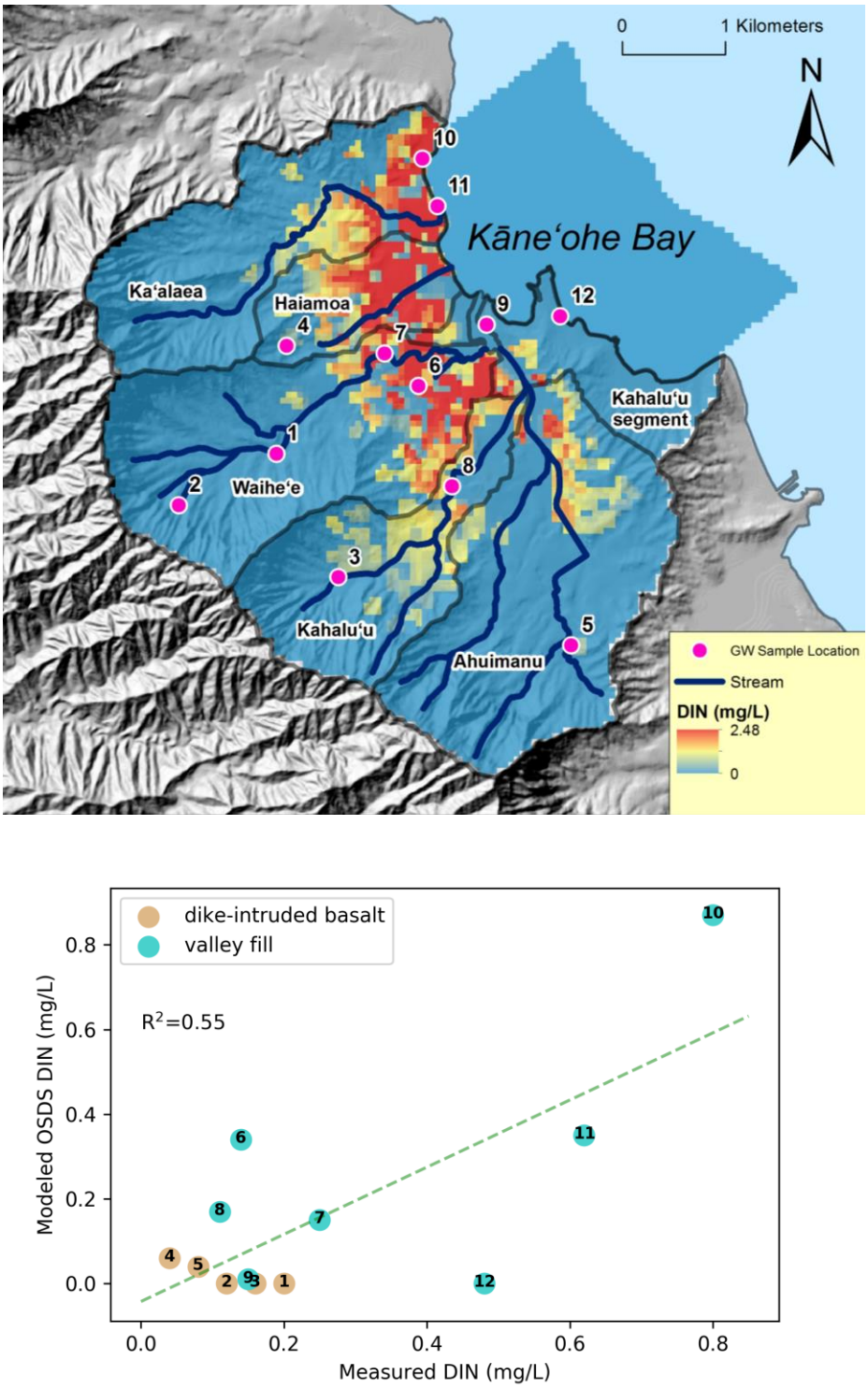

Figure 14: Steady-state results of MT3DMS simulation of groundwater OSDS dissolved inorganic nitrogen (DIN) concentrations (top). These steady state concentrations were reached after 30 years of OSDS input simulation. Groundwater sample points are marked as pink dots, and measured DIN from these locations is provided in Table 4, and plotted against modeled OSDS DIN (bottom).

5.0 DISCUSSION

5.1 Water budget excess

Based on the water budget calculations outlined in Section 4.1 and the modeling results presented in Section 4.4, the output excess for the study area (Ahuimanu, Kahaluʻu, Kahaluʻu segment, Waiheʻe, Haiamoa, and Kaʻalaea watersheds) is approximately 2.41 x 10^7 m^3/yr. More simply, the hydrologic outputs from this area (evapotranspiration, streamflow, pumping, SGD) exceed the hydrologic inputs (precipitation) by 45.6% (see **Table 5**). As mentioned in Section 4.2 and Section 4.4, the most likely explanation for this is that high-elevation groundwater stored in the dike complex, which is not accounted for by ongoing precipitation in the study area watersheds, is being drawn down to sustain streamflow. Four of the five study area streams (Ahuimanu, Kahaluʻu, Waiheʻe, Kaʻalaea) are sourced by this high-elevation groundwater, and all but one (Kaʻalaea) shows a significant excess of outputs relative to inputs. The idea, first proposed by Takasaki and Mink (1985), is that since windward valleys deeply penetrate the dike-impounded reservoir whereas leeward valleys do not, proportionately more dike-impounded groundwater is delivered to the windward aquifers from the area underneath the Koʻolau crest, and thus the natural groundwater divide lies leeward of the crest and not along it (see Hunt, 1996 aquifer delineations). As a result, significant quantities of discharge from the dike-impounded reservoir become relatively high elevation sources of baseflow to windward streams. The groundwater portion of the water budget, and a comparison with the modeled values, is presented in **Table 6**.

Table 5: Study area water budget with inputs (i.e., sources) assigned positive values and outputs (i.e., sinks) assigned negative values. The outputs exceed the inputs by 45.6%, suggesting the presence of an additional source of water to the system, which we conclude is likely high-level groundwater from the leeward side of the Koʻolau Mountains.

Source / Sink	Literature Flux (m^3/yr)	% of Input	Literature source
Precipitation	5.29×10^7*	--	Giambelluca (2013)
Evapotranspiration	-2.66×10^7*	50.3%	Giambelluca (2013)
Baseflow	-1.48×10^7	28.0%	Engott et al. (2015) and USGS Gauge Data
Runoff	-1.05×10^7	19.8%	Engott et al. (2015)
Pumping	-1.12×10^7	21.2%	Pumping records
SGD (fresh)	-1.39×10^7	26.3%	Dulai et al. (2016)
REMAINDER	**-2.41×10^7**	**-45.6%**	

Table 6: Study area groundwater budget with inputs (i.e., sources) assigned positive values and outputs (i.e., sinks) assigned negative values. The outputs exceed the inputs by 152.6% for literature values, and the modeled flux necessary to match stream baseflow and pumping (see Section 4.4) is considered the model deficit, which is 122.8%. This again suggests the presence of an additional source of water to the system, which we conclude is likely high-level groundwater from the leeward side of the Koʻolau Mountains. The 122.8% deficit in the model was made up for by adding a specified flux across the Koʻolau ridgeline of 1.94×10^7 m^3/yr.

Source / Sink	Literature Flux (m^3/yr)	Model Flux (m^3/yr)	Literature source
Recharge	1.58×10^7		Engott et al. (2015)
Baseflow	-1.48×10^7	-1.55×10^7	Engott et al. (2015) and USGS Gauge Data
Pumping	-1.12×10^7	-8.53×10^6	Pumping records
SGD (fresh)	-1.39×10^7	-1.12×10^7	Dulai et al. (2016)
REMAINDER	**-2.41×10^7**	**-1.94×10^7**	

Dulai et al. (2016) measured total SGD with radon (total SGD = 6.17×10^6 m^3/yr) and radium (6.34×10^7 m^3/yr) isotopes for our study area (values calculated based on a per meter of shoreline estimates from Dulai et al., 2016). An average of these values, paired with the assumption that the salty fraction of SGD in Hawaiʻi is 40-80% (60% is assumed for the calculation) of the total SGD (Street et al., 2008; Glenn et al., 2013; Mayfield, 2013; Kleven, 2014), results in a fresh SGD estimate of 1.39×10^7 m^3/yr, which is well within range of the model SGD flux of 1.12×10^7 m^3/yr.

5.2 Nutrients in streams

Dissolved silica is very prevalent in Hawaiian groundwater, being sourced from the weathering of Hawaiian basalts, which are approximately 46.5 - 49.4% silica by weight (Macdonald et al., 1983). The notable inverse correlation observed between silica and streamflow (Figure 8) confirms that under baseflow conditions the streams are being fed by groundwater, and during high flow conditions the groundwater component of streamflow is diluted by overland flow. Higher TN, TP, and DON concentrations during high flow signifies that high flow events transport large quantities of organic material to the streams. This organic material could be partially sourced from overflowing cesspools, as a moderate correlation (0.53) also exists between ammonia+ammonium and streamflow.

5.3 Hydraulic conductivity and contaminant transport

Oki (2005) suggests that marine and terrestrial valley fill may act as a barrier to groundwater flow in dike-free volcanic aquifers. Dikes, however, can significantly decrease the permeability of volcanic aquifers, resulting in a scenario whereby alluvial valley fill is more hydraulically conductive than the surrounding and underlying volcanic substrate. Our study clearly demonstrates that this is the condition for the Kahaluʻu study area, and indeed perhaps many of the aquifers that drain into and potentially threaten Kāneʻohe Bay. Our model-calibrated horizontal hydraulic conductivity (HK) value for dike-complex basalt (0.11 m/d) is an order of magnitude lower than our model-calibrated valley fill HK (1.75 m/d). Literature values for Hawaiian dike complex basalt range from 0.00003 to 1500 m/d, estimated primarily from pumping tests and hydrologic models (Todd, 1980; Hunt, 1996; Rotzoll and El-Kadi, 2008). Literature values for alluvial/saprolitic valley fill range from 0.02 m/d up to 150 m/d (Hunt, 1996; Oki, 2005), with the variance based primarily on age of deposits. Most estimates tend towards values <1 m/d. The wide range of values in both consolidated and unconsolidated Hawaiian aquifer materials is attributed to the heterogeneity of the subsurface structures on a local and island-wide scale, and the unknown and varying density of dikes that terminate below the surface. While numerous studies have mapped surface dike features within the Kahaluʻu study area (Macdonald et al., 1983; Takasaki and Mink, 1985; Walker, 1986; Walker, 1987), the density of dikes that terminate below the surface is entirely unknown. The low dike complex HK value obtained from our model calibration suggests that the

subsurface dike density in the study area is very high, impeding groundwater flow to the extent of decreasing flow by several orders of magnitude. This is not surprising since the study area is within the East Rift Zone and adjacent to the caldera of the Koʻolau volcano, where dike density is expected to be greatest. This result, along with the UAV-TIR mapping, supports the hypothesis that the valley fill is acting as a preferential subsurface flow conduit that funnels OSDS contaminants to streams and the coast. This is of significant concern since most of the OSDS within the study area are located within the alluvial portion of the valley fill. In addition, the northwest trending ridge that branches off from the main Koʻolau Crest up to the coast north of the fishpond (see Figure 1), where several surficial dike features have been mapped, likely acts as a barrier for groundwater flow, channeling subsurface flow towards the Kahaluʻu estuary and the surrounding alluvial floodplains, where we have delineated multiple nutrient-rich groundwater seeps by UAV-TIR and salinity measurements (Figure 12 and Appendix A). This unique hydrogeologic dynamic, coupled with high OSDS density, is a reasonable conclusion for the high groundwater, surface water, and SGD seep DIN concentrations in the area, which are the highest of any locations sampled as part of this study.

5.4 Gaining stream reaches

As noted in Section 4.1, Waiheʻe Stream is primarily fed by high-elevation groundwater, as evidenced by the fact that stream discharge values under baseflow conditions are relatively equivalent at our downstream gauge (19 m above msl) and the upstream USGS gauge (49 m above msl), over a distance of 1.3 km. The most significant area of gaining stream in Waiheʻe is immediately upstream of our stream gauge, where groundwater gains of 25 and 24 m^3/d per meter of stream length were measured for the wet and dry seasons, respectively. 27 OSDS are located within 200 m of this gaining stream segment. No OSDS systems are located upstream of the USGS gauge where most groundwater gains occur. Kahaluʻu stream is also gaining most of its flow upstream of the USGS gauge, but a majority (113 of 207) of the OSDS in the Kahaluʻu watershed are located in this region. Thus, gaining stream reaches are a much greater concern in Kahaluʻu stream than in Waiheʻe stream. In general, groundwater inputs to low-elevation stream reaches, where upgradient OSDS are present, are approximately 2.36×10^6 m^3/yr and

1.34 x 10^6 m^3/yr for Kahaluʻu and Waiheʻe streams, respectively. Some of this water is returned to the aquifer in losing stream reaches, but most is transported to the coast. With a high number of OSDS in close proximity to streams in the study area, groundwater inputs to streams can act as critical transport paths for OSDS contaminants to reach streams and eventually the coast. Without a sufficient buffering distance between sources (OSDS) and sinks (e.g., gaining stream reaches), there is little opportunity for natural attenuation of contaminants to occur via sorption, biodegradation, and decay. The streams in the study area are fast-moving, and once contaminants reach the streams, they can be quickly transported to the coast.

5.5 Areas of concern

Since we find groundwater flow in Kahaluʻu to be relatively slow, OSDS contaminants that reach streams or the coast in the immediate aftermath of a storm event are likely either sourced from near-shore or near-stream OSDS, with perhaps some transport also via overland flow after a system overflow or groundwater inundation. Based on an apparent groundwater input delineated by UAV-TIR, OSDS proximity, and high nutrient concentrations in near-shore wells and surface waters, the northeastern coastline of the Kahaluʻu estuary (estuarine confluence of Kahaluʻu, Ahuimanu, and Waiheʻe streams) is an area of concern. Likewise of concern are the coastal areas immediately northwest of the Kahaluʻu estuary ocean input (Appendix A), which have the lowest temperatures of any non-stream input area of the study area, as well as the highest nutrient concentrations of any coastal location sampled. As mentioned in the previous section, the stream reach immediately upstream of the Kahaluʻu USGS gauge (101 OSDS within 200 meters of the stream), as well as the stream reach immediately upstream of our Waiheʻe gauge (27 OSDS within 200 meters of the stream) are inland areas of concern due to the high quantity of groundwater input and the number of OSDS units in close proximity. The highest modeled OSDS DIN concentrations are in the low-lying areas and coastlines between Haiamoa Stream and the northern boundary of the Kaʻalaea watershed. Five of the eight SGD seeps occur in this area, where 53 OSDS are located within 50 meters of the coast, and 124 within 200 meters. Of all coastal locations, this

area and the aforementioned Kahaluʻu estuary coastal region (see Section 5.3) are the most significant areas of concern for potential OSDS contamination.

5.6 Future research

This study provides preliminary analysis of the hydrologic cycling of OSDS contaminants in the unique region of Windward Oʻahu. Due to the extreme spatial variability in subsurface structure and hydrologic/climatic forcing throughout the Hawaiian Islands, this study should not be considered representative of areas of Hawaiʻi outside the Windward Oʻahu study area. However, this study outlines a framework that is easily replicated for other areas in Hawaiʻi and worldwide affected by anthropogenic contamination of coastal waters. Other areas of the Hawaiian Islands that contain a high spatial density of OSDS and would thus benefit from a new iteration of this study include Waialua (Oʻahu) and Upcountry Maui.

The results of this study suggest that inter-aquifer flows (specifically from the leeward crest of the Koʻolau range to the windward side) may be a dominant mechanism of hydrologic cycling in Windward Oʻahu, but additional hydrologic data such as water levels, boring logs, geophysics, and pumping test data could help confirm this hypothesis and significantly increase our understanding of this critical region for water resources sustainability. Since our study was primarily concerned with contaminant transport from OSDS sources on land to streams and the sea, and many complicating factors and uncertainties were involved in the modeling, it was deemed unnecessary to add another dimension of complexity and uncertainty with density-dependent model inputs, such as the marine substrate and the depth to the freshwater-saltwater transition zone. If additional studies are conducted to gather this information, a density-dependent model (e.g., SEAWAT) could be utilized to gain a better understanding of how freshwater-saltwater dynamics in the subterranean estuary affect contaminant transport and hydrologic cycling in the coastal environment.

6.0 CONCLUSIONS

Model results demonstrate that valley fill is the most hydrologically conductive substrate in the study area, and the dike-intruded basalt, which is approximately 16 times less conductive than the valley fill, acts as a subsurface flow barrier. 87% of the OSDS in Kahaluʻu are located in alluvial valley fill sediments, and the valley fill is likely acting as a direct conduit for OSDS contaminant flow to streams and the coast. Eight primary SGD seeps have been delineated from TIR and salinity data. All eight seeps are routed through unconsolidated sediment/valley fill substrate, and nutrient concentrations in these locations are consistently elevated well above ocean baseline concentrations (Figure 11). Modeled OSDS DIN and measured DIN concentrations suggest that extensive natural attenuation of DIN is occurring between OSDS point-sources and surface water bodies. However, in areas where OSDS exist in close proximity to streams or the coast, an insufficient buffer can decrease the potential for natural attenuation, and groundwater discharges can thus transport significant contaminant loads. Several locations like this exist in the study area, such as the Kahaluʻu estuary, the stream segments spanning from 19 to 22 and 43 to 75 m elevation in Waiheʻe and Kahaluʻu streams, respectively, and the coastal region between the stream outlet of Haiamoa and the northern extents of Kaʻalaea watershed. The elevated groundwater and surface water DIN concentrations in and around Kahaluʻu estuary, coupled with the unique hydrologic dynamics of the area, warrant further study.

This study presents groundwater flow and transport models for a critical region of windward Oʻahu, and demonstrates the first effective use of UAV-TIR as an independent reconnaissance and mapping tool for coastal submarine groundwater discharge. While A/C-TIR is an effective means for regional-scale mapping operations, UAV-TIR provides unmatched resolution and flight flexibility that is ideal for localized mapping. The combination of UAV-TIR, stream gauging seepage runs, geochemical analysis, and numerical modeling provides a framework to evaluate contaminant flow regimes and water quality impacts in areas affected by anthropogenic contamination of coastal waters.

APPENDIX A – Thermal Infrared Maps

Processed thermal mosaics from UAV-TIR flights are provided in the following pages. Imagery was collected on 18 and 19 August 2017 during AM low tides, and processed using the methods outlined in Section 3.3 and Figure 4. All data is ortho-projected in Universal Transverse Mercator (UTM) Zone 4 using the WGS-84 datum. Unique temperature scales were utilized for each mosaic to maximize contrast for optimum visualization of hydrologic features. Stream shapefiles were obtained from the Hawai‘i Office of Planning GIS database and OSDS locations were obtained from Whittier and El-Kadi (2009). Mosaics are presented from southernmost to northernmost.

Laenani Beach Park Area (Kahaluʻu Segment watershed)

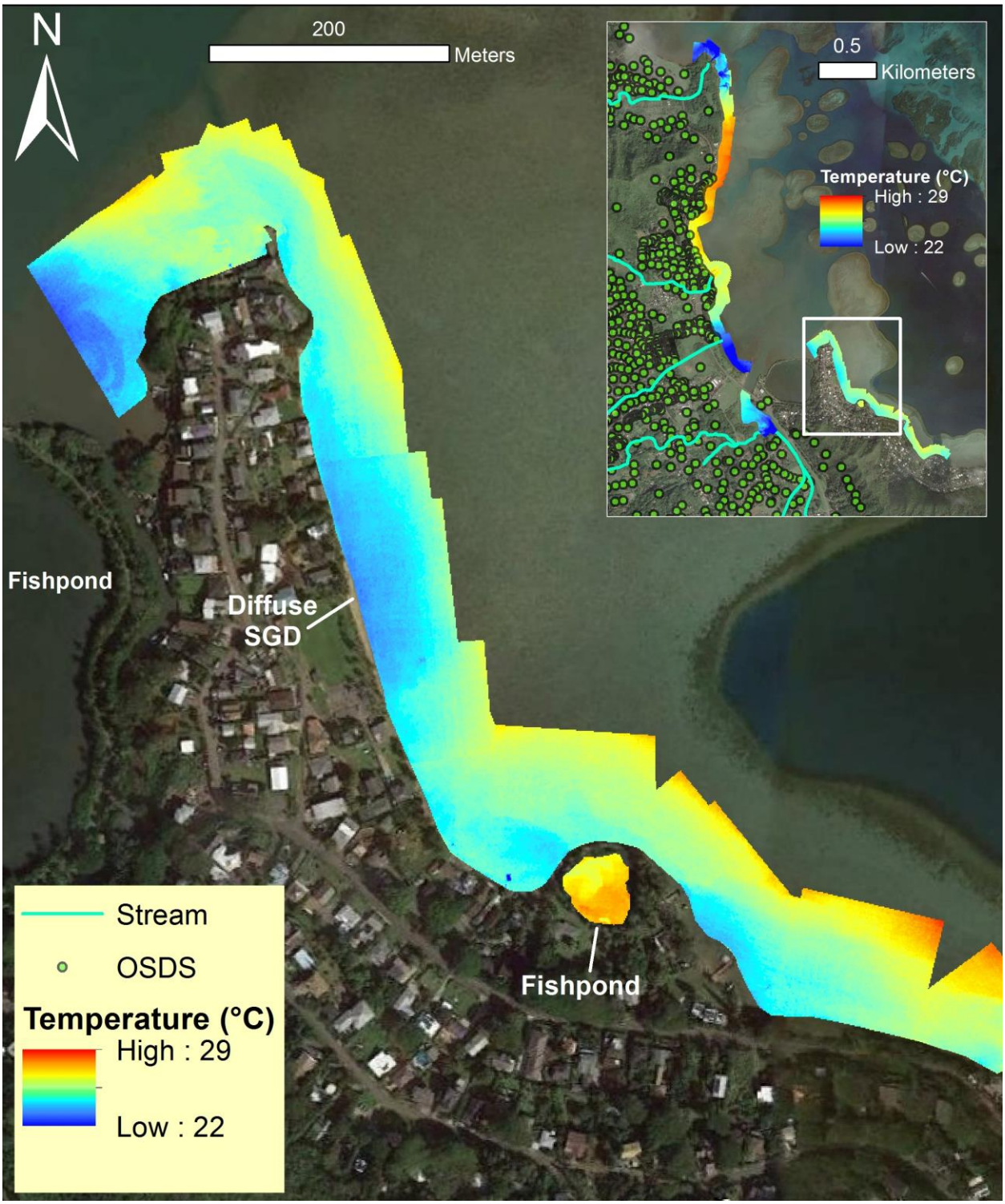

Kahaluʻu estuary (confluence of Ahuimanu / Kahaluʻu / Waiheʻe streams)

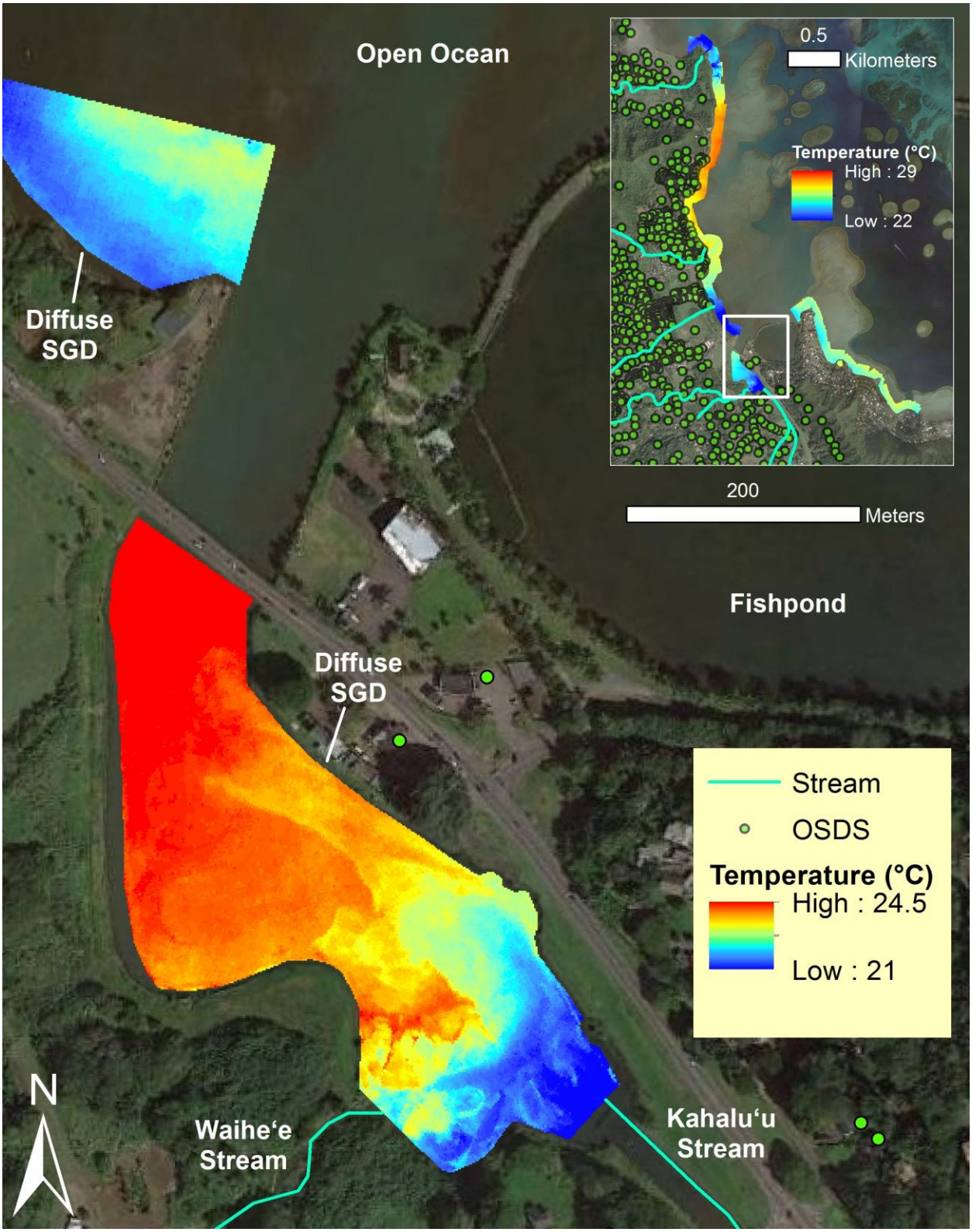

Kaʻalaea Stream Outlet and Surrounding Coastline (Kaʻalaea Watershed)

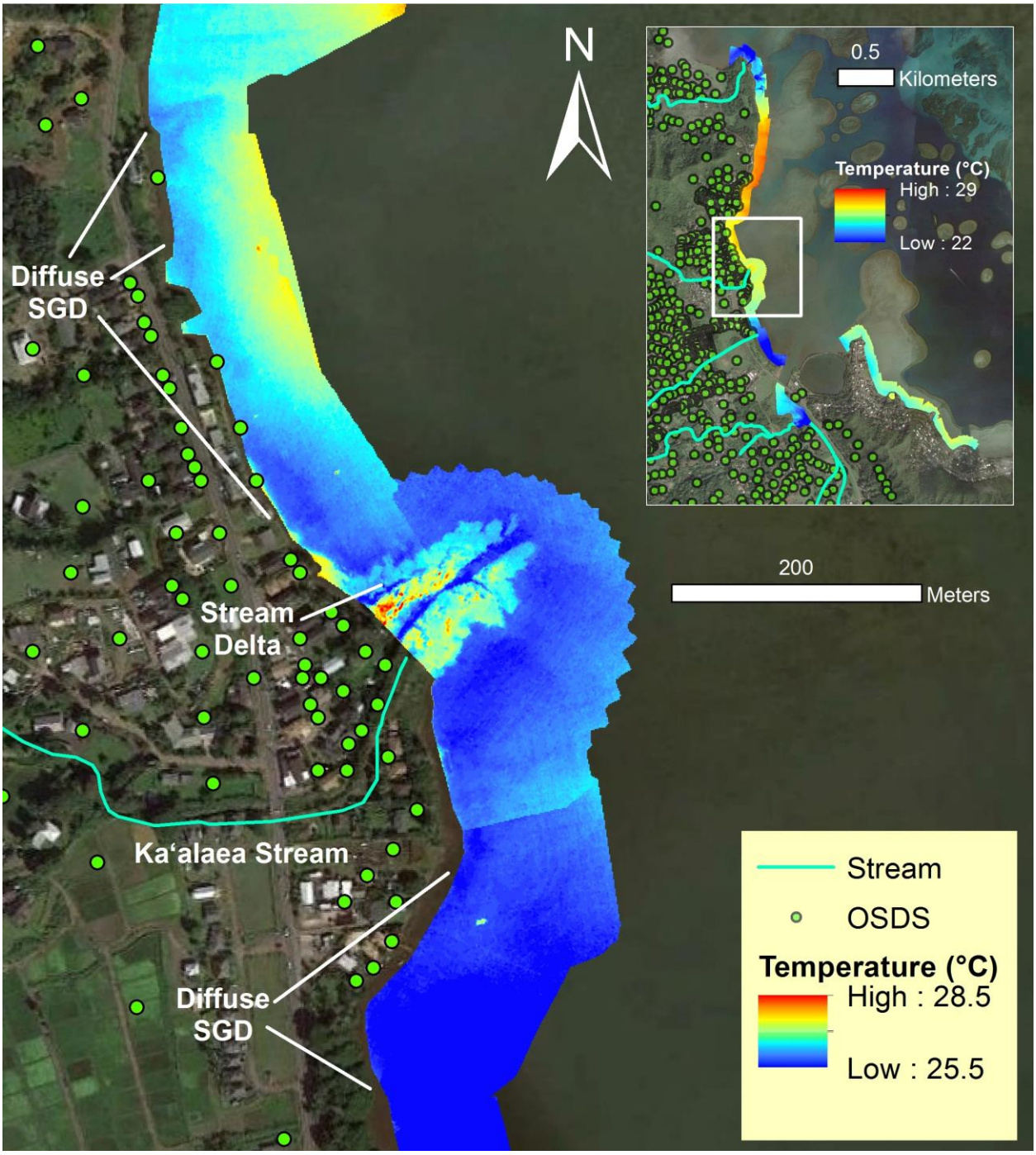

Northern Extent of Kaʻalaea Watershed / Southern Extent of Waiāhole Watershed

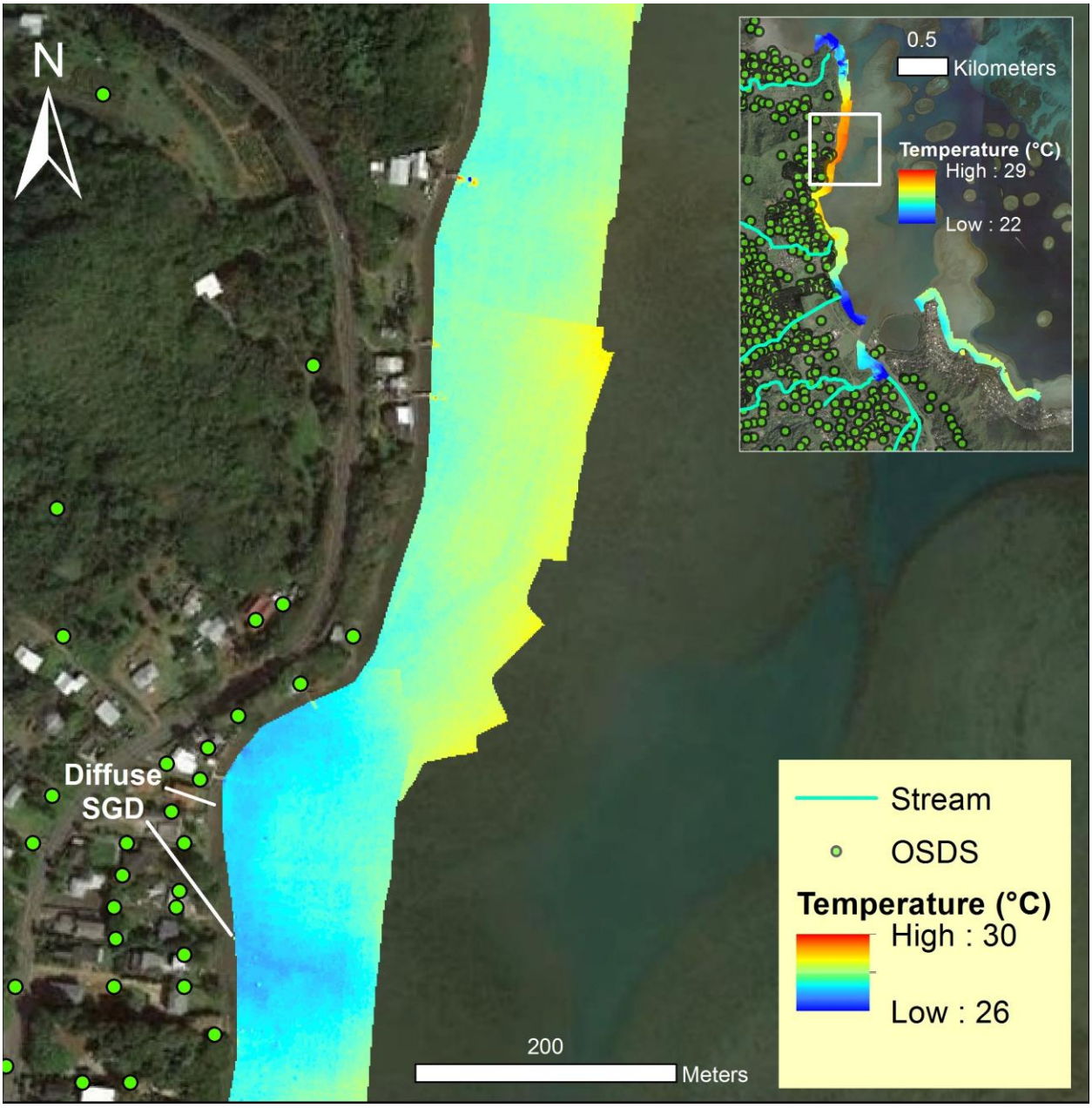

Waiāhole Stream Outlet and Surrounding Coastline (Waiāhole Watershed)

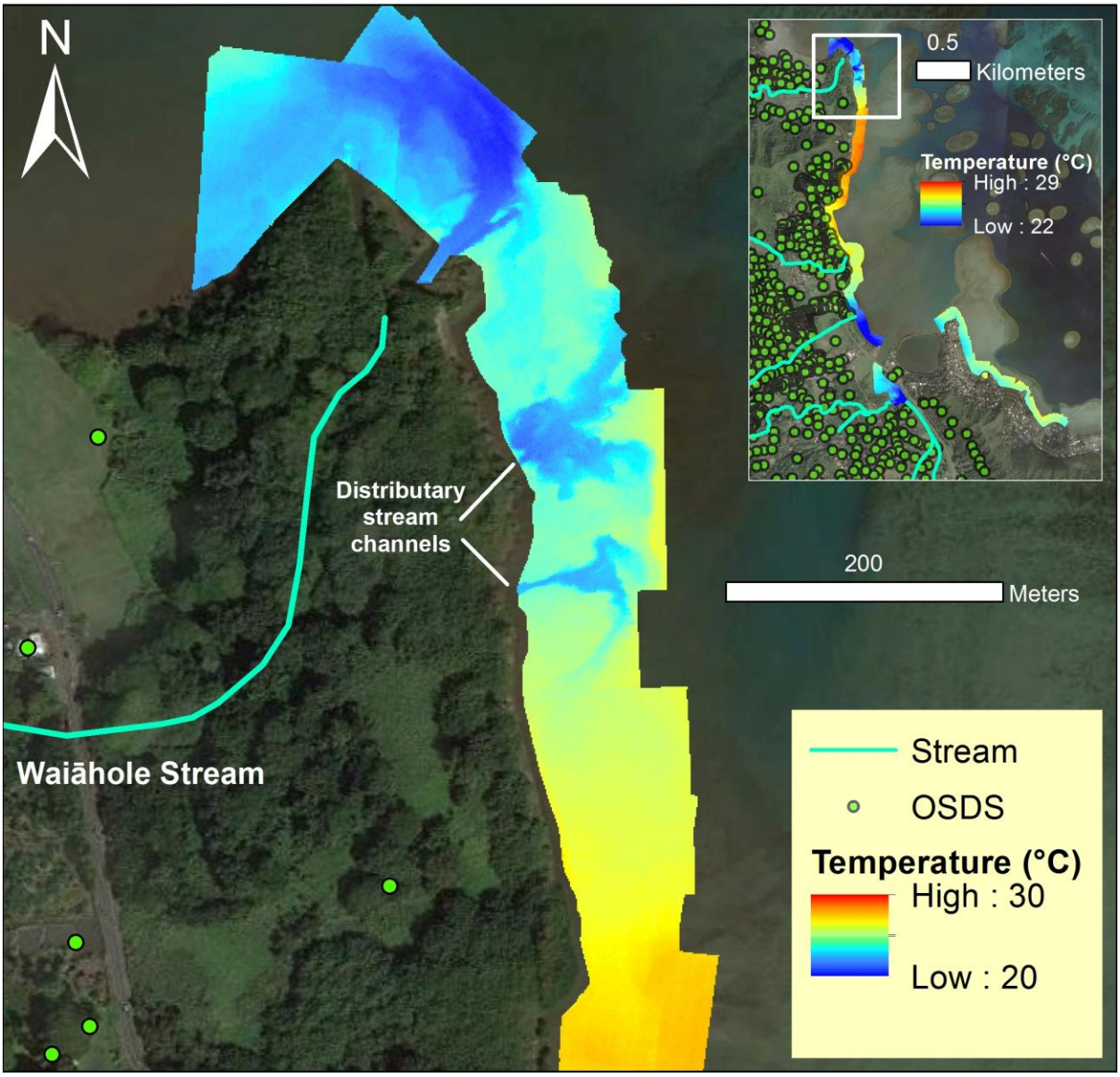

APPENDIX B – Streamflow Data

Summary of streamflow measurements throughout the study area and within the time period of March 2017 to May 2018.

Stream	Date	Time	Location	X (long)	Y (lat)	Flow (m^3/s)	Uncertainty
Haiamoa	4-Dec-2017	13:35	HAI-01	157.8473	21.4594	0.025	21.0
Kaalaea	4-Dec-2017	11:45	KAA-01	157.8430	21.4665	0.022	26.4
Kaalaea	4-Dec-2017	12:40	KAA-02	157.8548	21.4664	0.063	18.1
Kahaluu	6-Mar-2017	10:35	KAH-01	157.8419	21.4436	0.126	12.8
Kahaluu	10-Jul-2017	8:55				0.083	13.8
Kahaluu	6-Sep-2017	12:15				0.076	9.6
Kahaluu	20-Dec-2017	10:30				0.108	5.3
Kahaluu	26-Dec-2017	16:45				1.161	8.9
Kahaluu	26-Dec-2017	17:00				1.305	5.6
Kahaluu	28-Feb-2018	13:15				0.142	4.8
Kahaluu	6-Mar-2017	11:20	KAH-02	157.8420	21.4428	0.133	16.8
Kahaluu	10-Jul-2017	10:35				0.077	8.9
Kahaluu	6-Mar-2017	12:00	KAH-03	157.8423	21.4424	0.159	14.5
Kahaluu	10-Jul-2017	11:10				0.084	11.9
Kahaluu	6-Mar-2017	13:00	KAH-04	157.8427	21.4421	0.136	12.1
Kahaluu	10-Jul-2017	11:45				0.100	15.8
Kahaluu	6-Mar-2017	13:45	KAH-05	157.8425	21.4405	0.161	14.4
Kahaluu	10-Jul-2017	13:30				0.090	33.5
Kahaluu	6-Mar-2017	14:30	KAH-06	157.8435	21.4393	0.155	8.1
Kahaluu	10-Jul-2017	14:00				0.073	21.9
Kahaluu	6-Mar-2017	15:00	KAH-07	157.8438	21.4387	0.126	10.7
Kahaluu	10-Jul-2017	14:45				0.115	7.3
Kahaluu	6-Mar-2017	14:55	KAH-08	157.8436	21.4387	0.009	58.9
Kahaluu	10-Jul-2017	14:30				0.010	Unavailable
Kahaluu	26-May-2018	14:15	KAH-09	157.8493	21.4358	0.041	29.0
Waihee	11-Jul-2017	12:15	WAI-01	157.8432	21.4554	0.202	20.1
Waihee	1-Mar-2017	12:45	WAI-02	157.8481	21.4551	0.743	14.6
Waihee	22-Mar-2017	9:40				0.212	11.6
Waihee	12-Apr-2017	11:45				0.244	12.2
Waihee	11-Jul-2017	9:00				0.209	19.3

Stream	Date	Time	Location	X (long)	Y (lat)	Flow (m^3/s)	Uncertainty
Waihee	28-Feb-2018	11:45	WAI-02	157.8481	21.4551	0.306	10.9
Waihee	22-Mar-2017	10:50	WAI-03	157.8494	21.4547	0.172	9.5
Waihee	11-Jul-2017	14:25				0.171	15.2
Waihee	22-Mar-2017	11:47	WAI-04	157.8514	21.4526	0.200	9.8
Waihee	11-Jul-2017	16:35				0.160	6.2
Waihee	22-Mar-2017	12:36	WAI-05	157.8525	21.4520	0.182	16.0
Waihee	11-Jul-2017	16:55				0.169	21.0

APPENDIX C – Water Quality Parameters

Summary of water quality data collected throughout the study area and within the time period of October 2016 to April 2018.

Sample No.	Date	Time	Type	X (long)	Y (lat)	Temp (°C)	Salinity (psu)	pH	TDS	ODO (% sat)	ODO (mg/L)
1	7-Oct-2016	9:01	Estuary	157.8385	21.4570	23.93	2.04	7.37	--	89.1	--
2	7-Oct-2016	9:37	Estuary	157.8396	21.4601	24.26	5.04	7.35	--	100.2	--
3	7-Oct-2016	9:57	Estuary	157.8401	21.4590	24.25	4.39	7.46	--	93.2	--
4	7-Oct-2016	10:33	Estuary	157.8393	21.4562	24.77	1.29	7.82	--	112.3	--
5	7-Oct-2016	10:52	Estuary	157.8404	21.4577	25.47	2.75	7.57	--	111.2	--
6	7-Oct-2016	11:48	Stream	157.8452	21.4551	23.21	0.14	8.02	--	106.2	--
7	7-Oct-2016	12:18	Estuary	157.8380	21.4553	24.98	1.78	7.31	--	97.5	--
8	7-Oct-2016	12:45	Stream	157.8365	21.4545	29.32	2.16	7.16	--	94.9	--
9	7-Oct-2016	13:03	Stream	157.8345	21.4481	29.87	0.14	8.49	--	120.0	--
10	14-Oct-2016	9:18	Stream	157.8593	21.4459	23.71	0.05	8.59	--	101.2	--
11	14-Oct-2016	10:00	Stream	157.8323	21.4453	27.50	0.15	7.61	--	125.0	--
12	14-Oct-2016	10:16	Stream	157.8330	21.4462	26.05	0.13	8.01	--	115.2	--
13	14-Oct-2016	10:55	Stream	157.8375	21.4396	25.04	0.11	7.85	--	104.8	--
14	14-Oct-2016	11:28	Stream	157.8418	21.4435	22.96	0.10	7.77	--	102.9	--
15	14-Oct-2016	11:58	Stream	157.8436	21.4371	23.10	0.10	7.53	--	90.5	--
16	14-Oct-2016	12:17	Stream	157.8444	21.4386	20.87	0.10	7.08	--	89.1	--
17	23-Jan-2017	9:40	GW	157.8583	21.4464	19.82	0.07	--	100	100.9	9.21
18	23-Jan-2017	10:20	GW	157.8675	21.4419	19.33	0.04	--	63	97.6	8.99

Sample No.	Date	Time	Type	X (long)	Y (lat)	Temp (°C)	Salinity (psu)	pH	TDS	ODO (% sat)	ODO (mg/L)
19	25-Jan-2017	14:00	Stream	157.8521	21.4353	19.34	0.06	--	85	97.6	8.99
20	25-Jan-2017	14:30	GW	157.8526	21.4356	20.34	0.09	--	124	100.0	9.03
21	1-Mar-2017	9:45	Stream	157.8418	21.4436	--	--	--	--	--	--
22	1-Mar-2017	12:30	Stream	157.8482	21.4551	--	--	--	--	--	--
23	6-Mar-2017	10:25	Stream	157.8418	21.4436	20.82	0.08	7.85	114	98.1	8.77
24	6-Mar-2017	11:20	Stream	157.8421	21.4428	21.36	0.08	7.87	113	99.4	8.79
25	6-Mar-2017	12:00	Stream	157.8422	21.4423	21.56	0.08	7.88	113	99.3	8.75
26	6-Mar-2017	13:00	Stream	157.8431	21.4422	21.52	0.08	7.86	115	98.7	8.71
27	6-Mar-2017	13:45	Stream	157.8426	21.4406	21.35	0.09	7.86	129	99.1	8.77
28	6-Mar-2017	14:30	Stream	157.8437	21.4394	21.16	0.08	7.77	111	97.2	8.64
29	6-Mar-2017	15:00	Stream	157.8438	21.4387	21.06	0.08	7.77	108	98.3	8.75
30	20-Mar-2017	14:30	Stream	157.8482	21.4551	--	--	--	--	--	--
31	20-Mar-2017	14:35	GW	157.8482	21.4551	24.87	0.26	7.29	345	25.2	2.09
32	20-Mar-2017	15:30	Stream	157.8419	21.4434	21.67	0.08	7.82	111	96.3	8.48
33	20-Mar-2017	15:45	GW	157.8419	21.4434	23.19	0.10	7.32	135	88.3	7.55
34	22-Mar-2017	9:40	Stream	157.8482	21.4551	21.01	0.07	7.36	102	99.0	8.82
35	22-Mar-2017	10:50	Stream	157.8490	21.4551	21.63	0.07	7.83	100	101.7	8.95
36	22-Mar-2017	11:47	Stream	157.8515	21.4531	21.29	0.07	7.81	98	99.4	8.81
37	22-Mar-2017	12:36	Stream	157.8515	21.4532	21.18	0.07	7.94	98	97.5	8.66
37D	22-Mar-2017	12:36	Stream	157.8515	21.4532	21.18	0.07	7.94	98	97.5	8.66
38	22-Mar-2017	13:38	Stream	157.8527	21.4516	--	--	--	--	--	--
39	10-Jul-2017	9:00	Stream	157.8419	21.4434	21.74	0.08	8.02	112	95.4	8.38
39D	10-Jul-2017	9:00	Stream	157.8419	21.4434	21.74	0.08	8.02	112	95.4	8.38

Sample No.	Date	Time	Type	X (long)	Y (lat)	Temp (°C)	Salinity (psu)	pH	TDS	ODO (% sat)	ODO (mg/L)
40	10-Jul-2017	10:00	GW	157.8419	21.4434	23.39	0.09	7.52	126	50.4	4.27
41	10-Jul-2017	9:00	Porewater	157.8419	21.4434	22.50	0.08	7.96	114	93.5	8.10
42	10-Jul-2017	12:20	Stream	157.8431	21.4419	22.36	0.08	8.02	111	97.1	8.42
43	10-Jul-2017	12:20	Porewater	157.8431	21.4419	24.18	0.32	7.23	423	31.1	2.60
44	10-Jul-2017	14:30	Porewater	157.8437	21.4392	25.02	0.11	6.77	158	48.7	4.02
45	10-Jul-2017	15:00	Stream	157.8437	21.4394	22.17	0.08	7.97	109	98.7	8.60
46	10-Jul-2017	15:35	Stream	157.8437	21.4385	24.87	0.09	7.46	125	79.7	6.59
47	10-Jul-2017	15:30	Porewater	157.8437	21.4385	24.36	0.09	7.25	123	34.3	2.86
48	10-Jul-2017	16:05	Stream	157.8443	21.4385	21.80	0.08	7.87	107	95.6	8.38
49	10-Jul-2017	16:10	Porewater	157.8443	21.4385	22.48	0.08	7.87	108	91.8	7.95
50	10-Jul-2017	10:45	Stream	157.8421	21.4428	21.97	0.08	7.99	111	96.1	8.41
51	10-Jul-2017	11:20	Stream	157.8422	21.4423	22.03	0.08	8.01	111	97.4	8.51
52	10-Jul-2017	11:45	Stream	157.8431	21.4422	22.17	0.08	8.03	111	96.7	8.43
53	10-Jul-2017	12:55	Stream	157.8426	21.4406	22.67	0.08	8.06	110	97.1	8.38
54	10-Jul-2017	14:00	Stream	157.8437	21.4393	22.27	0.08	7.99	111	97.9	8.51
55	10-Jul-2017	13:20	Stream	157.8437	21.4394	22.65	0.13	8.06	179	98.7	8.51
56	11-Jul-2017	9:55	GW	157.8482	21.4551	24.34	0.15	7.39	203	23.8	1.96
57	11-Jul-2017	9:35	Stream	157.8482	21.4551	21.61	0.07	7.79	100	94.4	8.31
57D	11-Jul-2017	9:35	Stream	157.8482	21.4551	21.61	0.07	7.79	100	94.4	8.31
58	11-Jul-2017	9:00	Porewater	157.8482	21.4551	23.19	0.11	7.39	148	43.3	3.70
59	11-Jul-2017	10:25	Porewater	157.8475	21.4548	23.29	0.08	7.90	105	75.8	6.46
60	11-Jul-2017	10:20	Stream	157.8475	21.4548	21.90	0.07	7.90	100	96.0	8.41
61	11-Jul-2017	10:55	Stream	157.8460	21.4550	22.32	0.07	7.92	101	93.9	8.16

Sample No.	Date	Time	Type	X (long)	Y (lat)	Temp (°C)	Salinity (psu)	pH	TDS	ODO (% sat)	ODO (mg/L)
62	11-Jul-2017	11:30	Stream	157.8443	21.4547	22.74	0.07	7.94	102	95.0	8.19
63	11-Jul-2017	12:10	Stream	157.8432	21.4554	22.96	0.07	7.95	104	95.7	8.21
64	11-Jul-2017	12:50	Porewater	157.8430	21.4552	25.52	0.25	7.07	335	29.2	3.38
65	11-Jul-2017	13:00	Stream	157.8423	21.4553	--	--	--	--	--	--
66	11-Jul-2017	13:15	Stream	157.8419	21.4553	23.72	0.08	8.02	105	97.8	8.27
67	11-Jul-2017	13:55	Agriculture	157.8479	21.4549	--	--	--	--	--	--
68	11-Jul-2017	14:25	Stream	157.8491	21.4541	22.94	0.07	7.93	98	99.1	8.51
69	11-Jul-2017	15:45	Stream	157.8521	21.4533	21.34	0.07	8.01	96	95.2	8.42
70	11-Jul-2017	15:50	Porewater	157.8521	21.4533	22.67	0.09	6.69	127	19.0	1.63
71	11-Jul-2017	16:35	Stream	157.8519	21.4523	21.52	0.07	8.02	96	95.3	8.41
72	11-Jul-2017	16:55	Stream	157.8513	21.4531	21.70	0.07	7.86	97	93.3	8.20
73	13-Jul-2017	9:40	Estuary	157.8387	21.4559	29.11	11.62	7.79	12769	78.0	5.64
74	13-Jul-2017	9:50	Porewater	157.8387	21.4559	29.01	19.99	7.20	20922	13.8	0.95
74D	13-Jul-2017	9:50	Porewater	157.8387	21.4559	29.01	19.99	7.20	20922	13.8	0.95
75	13-Jul-2017	10:20	Estuary	157.8384	21.4555	26.64	7.77	7.34	8777	52.1	3.99
76	13-Jul-2017	10:30	Porewater	157.8384	21.4555	27.19	14.66	7.26	15754	28.3	2.06
77	13-Jul-2017	11:00	Porewater	157.8381	21.4555	28.11	3.70	6.72	4410	71.4	5.47
78	13-Jul-2017	11:40	Porewater	157.8381	21.4553	27.78	5.58	6.84	6470	33.8	2.59
79	13-Jul-2017	12:00	Porewater	157.8382	21.4558	27.91	14.21	6.99	15322	24.7	1.78
80	13-Jul-2017	12:30	Porewater	157.8388	21.4559	29.43	17.23	7.43	18290	33.3	2.31
81	13-Jul-2017	10:35	Estuary	157.8387	21.4554	23.35	0.29	8.05	392	86.5	7.35
82	13-Jul-2017	11:10	Estuary	157.8380	21.4554	27.52	3.65	7.50	4286	90.1	6.88
83	21-Aug-2017	9:26	Stream	157.8414	21.4447	23.23	0.09	8.25	120	107.8	9.20

Sample No.	Date	Time	Type	X (long)	Y (lat)	Temp (°C)	Salinity (psu)	pH	TDS	ODO (% sat)	ODO (mg/L)
84	21-Aug-2017	9:48	Porewater	157.8412	21.4447	23.58	0.10	7.06	138	70.8	6.00
85	21-Aug-2017	10:23	Stream	157.8377	21.4477	25.11	0.07	8.06	92	111.8	9.22
86	21-Aug-2017	10:32	Porewater	157.8377	21.4477	24.56	0.16	7.03	222	32.4	2.69
87	21-Aug-2017	10:54	Stream	157.8360	21.4507	25.15	0.08	7.72	112	109.9	9.07
88	21-Aug-2017	11:11	Porewater	157.8371	21.4484	25.16	0.18	7.14	241	34.7	2.85
89	21-Aug-2017	11:39	Stream	157.8351	21.4526	26.28	0.08	8.88	115	131.3	10.60
90	21-Aug-2017	11:45	Stream	157.8352	21.4528	28.40	0.08	9.10	111	127.1	9.87
91	21-Aug-2017	11:55	Stream	157.8355	21.4533	26.75	0.08	9.14	115	128.0	10.25
92	21-Aug-2017	12:02	Stream	157.8361	21.4540	27.48	0.31	9.14	423	134.8	10.64
93	22-Aug-2017	7:50	Ocean	157.8369	21.5089	27.62	34.76	8.25	34345	85.5	5.54
94	22-Aug-2017	8:15	Ocean	157.8443	21.4718	27.02	24.06	8.20	24692	80.5	5.60
95	22-Aug-2017	8:26	Ocean	157.8438	21.4700	27.18	23.51	8.17	24186	85.2	5.94
96	22-Aug-2017	8:40	Ocean	157.8398	21.4608	27.52	15.48	8.14	16559	90.7	6.57
96D	22-Aug-2017	8:40	Ocean	157.8398	21.4608	27.52	15.48	8.14	16559	90.7	6.57
97	22-Aug-2017	9:02	Ocean	157.8317	21.4590	28.11	32.57	8.27	32423	98.4	6.41
98	22-Aug-2017	9:13	Ocean	157.8256	21.4541	28.21	34.42	8.26	34065	94.7	6.10
99	22-Aug-2017	9:25	Ocean	157.8144	21.4500	28.36	34.69	8.32	34298	116.0	7.43
100	22-Aug-2017	9:34	Ocean	157.8201	21.4529	28.40	34.84	8.24	34431	94.6	6.06
101	30-Oct-2017	12:05	Ocean	157.8340	21.4593	26.03	18.93	--	--	--	--
102	31-Oct-2017	8:45	Stream	157.8459	21.4819	20.61	0.06	8.21	83	93.3	8.38
103	31-Oct-2017	9:15	Stream	157.8435	21.4665	24.79	0.13	7.87	183	76.2	6.31
104	31-Oct-2017	9:57	Stream	157.8430	21.4623	23.24	0.17	7.67	227	33.8	2.89
105	31-Oct-2017	10:25	Estuary	157.8404	21.4577	27.06	10.99	8.17	12420	94.2	7.11

Sample No.	Date	Time	Type	X (long)	Y (lat)	Temp (°C)	Salinity (psu)	pH	TDS	ODO (% sat)	ODO (mg/L)
105D	31-Oct-2017	10:25	Estuary	157.8404	21.4577	27.06	10.99	8.17	12420	94.2	7.11
106	31-Oct-2017	11:12	Stream	157.8489	21.4545	21.75	0.07	8.12	100	99.2	8.71
107	31-Oct-2017	11:55	Stream	157.8419	21.4435	22.77	0.08	8.20	117	96.0	8.31
108	3-Nov-2017	7:45	Stream	157.8381	21.4475	23.07	0.09	7.89	122	99.0	8.48
109	3-Nov-2017	8:05	Stream	157.8381	21.4528	23.75	0.12	8.27	160	113.6	9.60
110	3-Nov-2017	8:25	Stream	157.8333	21.4475	24.63	0.10	8.74	144	124.0	10.31
111	3-Nov-2017	9:00	Stream	157.8433	21.4375	22.75	0.07	7.63	103	63.2	5.44
112	4-Dec-2017	11:20	Stream	157.8431	21.4667	22.96	0.13	7.80	174	84.9	7.24
113	4-Dec-2017	11:40	Porewater	157.8431	21.4667	24.26	0.26	7.69	346	39.9	3.34
114	4-Dec-2017	12:40	Stream	-157.8549	21.4664	21.81	0.08	7.92	112	92.6	8.12
115	4-Dec-2017	13:35	Stream	157.8474	21.4596	23.22	0.13	8.16	176	84.6	7.21
116	5-Dec-2017	9:45	Ocean	157.8428	21.4683	21.04	28.30	8.44	28477	97.9	7.40
117	5-Dec-2017	10:16	Porewater	157.8431	21.4679	23.64	8.41	7.96	9416	51.5	4.15
118	5-Dec-2017	10:35	Porewater	157.8443	21.4698	22.71	23.36	7.76	23976	51.0	3.84
119	5-Dec-2017	10:48	Ocean	157.8442	21.4712	21.60	29.62	8.46	29670	96.3	7.13
120	5-Dec-2017	11:13	Porewater	157.8445	21.4721	23.01	0.66	7.35	857	69.1	5.90
121	5-Dec-2017	11:46	Ocean	157.8424	21.4732	21.79	30.25	8.50	30235	103.9	7.65
122	5-Dec-2017	11:57	Ocean	157.8430	21.4733	21.80	26.38	8.49	26738	101.2	7.62
123	11-Dec-2017	12:08	Ocean	157.8283	21.4610	24.85	34.69	8.53	34074	132.4	8.95
124	11-Dec-2017	12:48	Ocean	157.8292	21.4666	25.28	34.65	8.56	34194	125.4	8.48
125	11-Dec-2017	14:00	Porewater	157.8260	21.4541	25.49	10.91	7.97	12199	38.1	2.92
126	11-Dec-2017	15:02	Ocean	157.8308	21.4577	26.39	33.90	8.30	33579	83.2	5.52
127	11-Dec-2017	15:40	Porewater	157.8317	21.4582	25.31	1.44	7.72	1817	41.3	3.35

Sample No.	Date	Time	Type	X (long)	Y (lat)	Temp (°C)	Salinity (psu)	pH	TDS	ODO (% sat)	ODO (mg/L)
128	11-Dec-2017	16:04	Ocean	157.8319	21.4591	26.12	33.92	8.46	33600	106.5	7.11
129	11-Dec-2017	17:24	Ocean	157.8427	21.4647	26.97	29.23	8.40	28910	105.0	7.09
130	11-Dec-2017	18:12	Ocean	157.8416	21.4792	24.26	22.72	8.42	23397	91.5	6.73
131	20-Dec-2017	10:50	GW	157.8419	21.4434	21.24	0.10	7.64	133	73.6	6.52
131D	20-Dec-2017	10:50	GW	157.8419	21.4434	21.24	0.10	7.64	133		6.52
132	20-Dec-2017	12:17	Ocean	157.8408	21.4608	22.83	27.97	8.29	28193	80.8	5.92
133	20-Dec-2017	12:37	Stream	157.8433	21.4643	22.67	0.18	9.18	239	69.8	6.02
134D	20-Dec-2017	12:37	Stream	156.8433	22.4643	23.67	1.18	10.18	240	70.8	7.02
135	26-Dec-2017	17:20	Stream	157.8431	21.4419	20.68	0.14	--	--	--	--
136	1-Feb-2018	10:20	GW	157.8573	21.4558	23.60	0.11	7.98	149	58.1	4.92
137	1-Feb-2018	11:40	GW	157.8385	21.4575	25.72	0.12	8.01	169	42.7	3.39
137D	1-Feb-2018	12:20	GW	157.8385	21.4575	25.72	0.12	8.01	169	42.7	3.39
138	1-Feb-2018	13:15	GW	157.8388	21.4575	27.88	1.23	7.33	1570	30.9	2.35
139	1-Feb-2018	14:00	GW	157.8315	21.4292	23.49	0.08	7.90	111	68.1	5.77
140	2-Feb-2018	10:30	GW	157.8450	21.4522	23.66	0.09	7.39	130	82.8	7.01
140D	2-Feb-2018	10:30	GW	157.8450	21.4522	23.66	0.09	7.39	130	82.8	7.01
141	25-Sep-2017	10:00	Wastewater	157.7054	21.3388	29.35	0.35	7.61	468	35.8	2.72
142	25-Sep-2017	10:30	Wastewater	157.7054	21.3388	29.31	0.33	7.48	445	43.6	3.27
143	25-Sep-2017	10:45	Wastewater	157.7054	21.3388	29.32	0.49	7.72	657	36.3	2.74
144	28-Feb-2018	10:00	Septic	157.8390	21.4576	--	--	--	--	--	--
144D	28-Feb-2018	10:00	Septic	157.8390	21.4576	--	--	--	--	--	--
145	28-Feb-2018	10:00	Septic	157.8390	21.4576	--	--	--	--	--	--
146	28-Feb-2018	11:34	Stream	157.8418	21.4291	--	--	--	--	--	--

Sample No.	Date	Time	Type	X (long)	Y (lat)	Temp (°C)	Salinity (psu)	pH	TDS	ODO (% sat)	ODO (mg/L)
146D	28-Feb-2018	11:34	Stream	157.8418	21.4291	--	--	--	--	--	--
147	28-Feb-2018	11:52	Stream	157.8407	21.4298	--	--	--	--	--	--
148	28-Feb-2018	12:05	Stream	157.8390	21.4307	--	--	--	--	--	--
149	27-Apr-2018	9:00	Estuary	157.8390	21.4572	23.02	7.36	8.17	8326	84.9	7.00
150	27-Apr-2018	9:10	Estuary	157.8390	21.4573	22.97	5.19	8.51	6021	94.0	7.83
151	27-Apr-2018	9:30	Estuary	157.8390	21.4574	23.46	15.56	8.38	12977	76.0	5.89
152	27-Apr-2018	9:40	Estuary	157.8390	21.4577	23.47	9.04	8.42	9676	88.1	7.15
153	27-Apr-2018	10:30	Estuary	157.8339	21.4585	--	--	--	--	--	--
154	27-Apr-2018	11:00	Stream	157.8418	21.4433	21.47	0.08	8.45	108	93.7	8.28

APPENDIX D – Sample Results

Summary of analytical data collected throughout the study area and within the time period of October 2016 to April 2018. DON was calculated as the difference between Total N and DIN, which were run as separate laboratory analyses. Thus, any negative values are due to propagation of analytical error and should be considered equal to zero.

Sample No.	Date	Time	Type	X (long)	Y (lat)	Total P (uM P)	Total N (uM N)	NH_3+NH_4 (uM N)	NO_2+NO_3 (uM N)	DIN (uM N)	DON (uM N)	Si (uM)
1	7-Oct-2016	9:01	Estuary	157.8385	21.4570	0.77	12.85	2.21	11.57	13.92	-1.07	429
2	7-Oct-2016	9:37	Estuary	157.8396	21.4601	0.84	14.99	2.28	6.85	9.42	5.57	374
3	7-Oct-2016	9:57	Estuary	157.8401	21.4590	0.77	18.28	2.57	15.21	17.99	0.29	403
4	7-Oct-2016	10:33	Estuary	157.8393	21.4562	0.81	15.78	0.14	4.50	4.85	10.92	433
5	7-Oct-2016	10:52	Estuary	157.8404	21.4577	0.74	15.78	2.36	5.43	8.00	7.78	413
6	7-Oct-2016	11:48	Stream	157.8452	21.4551	0.81	9.50	0.14	6.85	7.07	2.43	499
7	7-Oct-2016	12:18	Estuary	157.8380	21.4553	0.77	15.71	2.14	6.35	8.71	7.00	451
8	7-Oct-2016	12:45	Stream	157.8365	21.4545	1.29	16.85	0.71	5.28	6.14	10.71	428
9	7-Oct-2016	13:03	Stream	157.8345	21.4481	0.45	18.28	1.00	6.64	7.78	10.49	413
10	14-Oct-2016	9:18	Stream	157.8593	21.4459	1.29	14.64	1.21	8.00	9.28	5.35	431
11	14-Oct-2016	10:00	Stream	157.8323	21.4453	0.32	7.07	0.29	0.36	0.71	6.35	428
12	14-Oct-2016	10:16	Stream	157.8330	21.4462	0.39	17.85	0.21	12.99	13.28	4.57	434
13	14-Oct-2016	10:55	Stream	157.8375	21.4396	0.48	16.49	0.14	7.35	7.57	8.92	479
14	14-Oct-2016	11:28	Stream	157.8418	21.4435	0.90	12.42	0.21	12.21	12.49	-0.07	499

Sample No.	Date	Time	Type	X (long)	Y (lat)	Total P (uM P)	Total N (uM N)	NH_3+NH_4 (uM N)	NO_2+NO_3 (uM N)	DIN (uM N)	DON (uM N)	Si (uM)
15	14-Oct-2016	11:58	Stream	157.8436	21.4371	0.36	34.41	0.36	33.63	34.06	0.36	343
16	14-Oct-2016	12:17	Stream	157.8444	21.4386	1.00	12.57	0.21	11.42	11.71	0.86	501
17	23-Jan-2017	9:40	GW	157.8583	21.4464	1.32	17.28	0.14	14.06	14.28	3.00	543
18	23-Jan-2017	10:20	GW	157.8675	21.4419	1.29	16.06	0.14	8.57	8.78	7.28	458
19	25-Jan-2017	14:00	Stream	157.8521	21.4353	1.13	17.42	0.21	11.64	11.92	5.50	444
20	25-Jan-2017	14:30	GW	157.8526	21.4356	1.42	17.56	0.14	11.57	11.78	5.78	579
21	1-Mar-2017	9:45	Stream	157.8418	21.4436	1.26	28.77	1.43	12.42	14.06	14.71	240
22	1-Mar-2017	12:30	Stream	157.8482	21.4551	0.97	21.56	0.86	5.35	6.28	15.28	356
23	6-Mar-2017	10:25	Stream	157.8418	21.4436	1.00	22.35	0.21	16.49	16.78	5.57	483
24	6-Mar-2017	11:20	Stream	157.8421	21.4428	0.87	21.20	0.29	15.92	16.28	4.93	484
25	6-Mar-2017	12:00	Stream	157.8422	21.4423	1.19	21.42	0.21	14.21	14.49	6.93	488
26	6-Mar-2017	13:00	Stream	157.8431	21.4422	0.94	19.70	0.21	15.21	15.49	4.21	484
27	6-Mar-2017	13:45	Stream	157.8426	21.4406	0.97	21.70	0.14	15.14	15.35	6.35	496
28	6-Mar-2017	14:30	Stream	157.8437	21.4394	0.90	19.63	1.07	14.71	15.85	3.78	489
29	6-Mar-2017	15:00	Stream	157.8438	21.4387	1.00	17.71	0.29	12.42	12.78	4.93	494
30	20-Mar-2017	14:30	Stream	157.8482	21.4551	0.87	9.28	0.36	7.00	7.43	1.86	488
31	20-Mar-2017	14:35	GW	157.8482	21.4551	0.42	19.78	16.78	1.21	18.06	1.71	558
32	20-Mar-2017	15:30	Stream	157.8419	21.4434	0.84	17.99	0.14	14.06	14.28	3.71	484
33	20-Mar-2017	15:45	GW	157.8419	21.4434	4.58	16.35	2.36	11.35	16.35	0.00	528
34	22-Mar-2017	9:40	Stream	157.8482	21.4551	0.84	9.71	0.50	3.50	4.07	5.64	491
35	22-Mar-2017	10:50	Stream	157.8490	21.4551	1.10	8.64	0.29	6.28	6.64	2.00	486
36	22-Mar-2017	11:47	Stream	157.8515	21.4531	0.97	22.99	0.14	10.14	10.35	12.64	488
37	22-Mar-2017	12:36	Stream	157.8515	21.4532	1.19	13.85	0.21	8.07	8.35	5.50	489

Sample No.	Date	Time	Type	X (long)	Y (lat)	Total P (uM P)	Total N (uM N)	NH_3+NH_4 (uM N)	NO_2+NO_3 (uM N)	DIN (uM N)	DON (uM N)	Si (uM)
37D	22-Mar-2017	12:36	Stream	157.8515	21.4532	1.03	23.06	0.14	11.78	11.99	11.07	484
38	22-Mar-2017	13:38	Stream	157.8527	21.4516	1.10	10.99	0.36	6.57	7.00	4.00	486
39	10-Jul-2017	9:00	Stream	157.8419	21.4434	0.81	32.70	0.14	11.42	11.64	21.06	546
39D	10-Jul-2017	9:00	Stream	157.8419	21.4434	1.00	29.70	0.21	11.71	11.99	17.71	548
40	10-Jul-2017	10:00	GW	157.8419	21.4434	0.39	5.50	1.00	0.71	1.78	3.71	596
41	10-Jul-2017	9:00	Porewater	157.8419	21.4434	0.94	28.06	0.14	10.49	10.71	17.35	549
42	10-Jul-2017	12:20	Stream	157.8431	21.4419	0.84	24.92	0.29	10.07	10.42	14.49	551
43	10-Jul-2017	12:20	Porewater	157.8431	21.4419	0.61	35.13	34.98	1.93	37.13	-2.00	408
44	10-Jul-2017	14:30	Porewater	157.8437	21.4392	0.32	3.28	0.57	0.29	0.93	2.36	807
45	10-Jul-2017	15:00	Stream	157.8437	21.4394	0.94	23.70	0.21	9.78	10.07	13.64	551
46	10-Jul-2017	15:35	Stream	157.8437	21.4385	0.94	50.12	2.43	41.62	44.34	5.78	458
47	10-Jul-2017	15:30	Porewater	157.8437	21.4385	0.55	52.12	3.57	12.49	16.42	35.70	443
48	10-Jul-2017	16:05	Stream	157.8443	21.4385	0.90	--	0.64	9.92	10.64	--	549
49	10-Jul-2017	16:10	Porewater	157.8443	21.4385	0.97	--	0.57	10.85	11.49	--	551
50	10-Jul-2017	10:45	Stream	157.8421	21.4428	0.72	11.70	0.18	9.18	9.36	2.34	567
51	10-Jul-2017	11:20	Stream	157.8422	21.4423	1.05	13.53	1.09	10.27	11.36	2.17	566
52	10-Jul-2017	11:45	Stream	157.8431	21.4422	0.94	12.22	0.61	10.03	10.64	1.58	569
53	10-Jul-2017	12:55	Stream	157.8426	21.4406	0.97	12.78	1.12	9.94	11.06	1.72	570
54	10-Jul-2017	14:00	Stream	157.8437	21.4393	0.93	12.48	0.15	10.48	10.63	1.85	570
55	10-Jul-2017	13:20	Stream	157.8437	21.4394	0.95	15.03	1.29	11.86	13.15	1.88	573
56	11-Jul-2017	9:55	GW	157.8482	21.4551	2.26	--	13.21	0.71	14.28	--	627
57	11-Jul-2017	9:35	Stream	157.8482	21.4551	0.90	10.28	0.57	5.85	6.50	3.78	538
57D	11-Jul-2017	9:35	Stream	157.8482	21.4551	0.87	10.00	1.29	6.21	7.57	2.43	538

Sample No.	Date	Time	Type	X (long)	Y (lat)	Total P (uM P)	Total N (uM N)	NH_3+NH_4 (uM N)	NO_2+NO_3 (uM N)	DIN (uM N)	DON (uM N)	Si (uM)
58	11-Jul-2017	9:00	Porewater	157.8482	21.4551	1.00	5.50	0.86	2.07	3.00	2.50	597
59	11-Jul-2017	10:25	Porewater	157.8475	21.4548	1.10	9.35	0.93	6.28	7.28	2.07	538
60	11-Jul-2017	10:20	Stream	157.8475	21.4548	1.23	12.99	1.29	10.49	11.92	1.07	523
61	11-Jul-2017	10:55	Stream	157.8460	21.4550	1.61	9.07	0.86	6.78	7.85	1.21	536
62	11-Jul-2017	11:30	Stream	157.8443	21.4547	1.78	7.21	0.93	5.64	6.78	0.43	536
63	11-Jul-2017	12:10	Stream	157.8432	21.4554	4.84	--	205.62	0.36	206.33	--	699
64	11-Jul-2017	12:50	Porewater	157.8430	21.4552	1.42	12.78	1.93	5.21	7.35	5.43	536
65	11-Jul-2017	13:00	Stream	157.8423	21.4553	2.45	13.07	14.99	0.07	15.14	-2.07	712
66	11-Jul-2017	13:15	Stream	157.8419	21.4553	1.65	4.85	0.64	4.43	5.28	-0.43	533
67	11-Jul-2017	13:55	Agriculture	157.8479	21.4549	19.53	38.84	7.14	23.20	32.13	6.71	536
68	11-Jul-2017	14:25	Stream	157.8491	21.4541	1.03	9.92	0.71	5.50	6.28	3.64	528
69	11-Jul-2017	15:45	Stream	157.8521	21.4533	1.07	4.21	0.14	7.64	7.85	-3.64	527
70	11-Jul-2017	15:50	Porewater	157.8521	21.4533	0.84	1.78	0.36	0.21	0.64	1.14	760
71	11-Jul-2017	16:35	Stream	157.8519	21.4523	1.19	7.07	0.36	7.00	7.43	-0.36	530
72	11-Jul-2017	16:55	Stream	157.8513	21.4531	1.10	13.21	0.21	7.00	7.28	5.93	525
73	13-Jul-2017	9:40	Estuary	157.8387	21.4559	3.68	15.92	3.28	3.50	7.14	8.78	303
74	13-Jul-2017	9:50	Porewater	157.8387	21.4559	1.58	--	13.92	0.43	14.49	--	273
74D	13-Jul-2017	9:50	Porewater	157.8387	21.4559	1.58	--	14.64	0.29	14.99	--	268
75	13-Jul-2017	10:20	Estuary	157.8384	21.4555	3.39	28.91	18.92	2.93	22.13	6.78	398
76	13-Jul-2017	10:30	Porewater	157.8384	21.4555	3.52	--	69.97	0.07	70.11	--	341
77	13-Jul-2017	11:00	Porewater	157.8381	21.4555	0.68	12.99	0.36	6.93	7.35	5.64	568
78	13-Jul-2017	11:40	Porewater	157.8381	21.4553	3.16	--	26.42	0.07	26.56	--	541
79	13-Jul-2017	12:00	Porewater	157.8382	21.4558	0.77	--	22.85	0.07	22.99	--	361

Sample No.	Date	Time	Type	X (long)	Y (lat)	Total P (uM P)	Total N (uM N)	NH_3+NH_4 (uM N)	NO_2+NO_3 (uM N)	DIN (uM N)	DON (uM N)	Si (uM)
80	13-Jul-2017	12:30	Porewater	157.8388	21.4559	7.10	--	159.92	0.07	160.07	--	320
81	13-Jul-2017	10:35	Estuary	157.8387	21.4554	1.99	17.82	3.25	8.40	11.65	6.17	526
82	13-Jul-2017	11:10	Estuary	157.8380	21.4554	1.41	13.33	3.39	5.40	8.79	4.54	476
83	21-Aug-2017	9:26	Stream	157.8414	21.4447	--	--	1.86	5.43	7.43	--	511
84	21-Aug-2017	9:48	Porewater	157.8412	21.4447	--	--	2.71	2.21	5.00	--	511
85	21-Aug-2017	10:23	Stream	157.8377	21.4477	--	--	5.93	0.86	7.00	--	373
86	21-Aug-2017	10:32	Porewater	157.8377	21.4477	--	--	8.92	0.07	9.07	--	484
87	21-Aug-2017	10:54	Stream	157.8360	21.4507	--	--	4.14	1.43	5.71	--	471
88	21-Aug-2017	11:11	Porewater	157.8371	21.4484	--	--	19.28	0.07	19.42	--	539
89	21-Aug-2017	11:39	Stream	157.8351	21.4526	--	--	9.28	0.14	9.57	--	478
90	21-Aug-2017	11:45	Stream	157.8352	21.4528	--	--	1.43	0.36	1.93	--	374
91	21-Aug-2017	11:55	Stream	157.8355	21.4533	--	--	1.07	0.50	1.71	--	463
92	21-Aug-2017	12:02	Stream	157.8361	21.4540	--	--	2.50	0.36	2.93	--	421
93	22-Aug-2017	7:50	Ocean	157.8369	21.5089	0.55	--	0.14	0.14	0.36	--	8
94	22-Aug-2017	8:15	Ocean	157.8443	21.4718	1.13	--	1.78	0.07	1.93	--	73
95	22-Aug-2017	8:26	Ocean	157.8438	21.4700	1.03	--	1.00	0.07	1.14	--	68
96	22-Aug-2017	8:40	Ocean	157.8398	21.4608	0.97	--	3.14	2.36	5.71	--	251
96D	22-Aug-2017	8:40	Ocean	157.8398	21.4608	1.00	--	3.71	3.00	6.93	--	262
97	22-Aug-2017	9:02	Ocean	157.8317	21.4590	0.77	--	1.00	0.07	1.14	--	26
98	22-Aug-2017	9:13	Ocean	157.8256	21.4541	0.65	--	1.36	0.14	1.57	--	14
99	22-Aug-2017	9:25	Ocean	157.8144	21.4500	0.39	--	0.57	0.07	0.71	--	10
100	22-Aug-2017	9:34	Ocean	157.8201	21.4529	0.61	--	1.07	0.07	1.21	--	9
101	30-Oct-2017	12:05	Ocean	157.8340	21.4593	0.90	25.63	12.49	6.21	19.99	5.64	21

Sample No.	Date	Time	Type	X (long)	Y (lat)	Total P (uM P)	Total N (uM N)	NH_3+NH_4 (uM N)	NO_2+NO_3 (uM N)	DIN (uM N)	DON (uM N)	Si (uM)
102	31-Oct-2017	8:45	Stream	157.8459	21.4819	0.61	10.42	1.50	4.71	6.28	4.14	491
103	31-Oct-2017	9:15	Stream	157.8435	21.4665	1.03	34.20	4.36	12.57	16.99	17.21	297
104	31-Oct-2017	9:57	Stream	157.8430	21.4623	1.39	35.41	2.43	13.35	15.85	19.56	246
105	31-Oct-2017	10:25	Estuary	157.8404	21.4577	0.84	13.21	5.64	2.14	8.00	5.21	180
105D	31-Oct-2017	10:25	Estuary	157.8404	21.4577	0.55	10.49	4.43	3.86	8.50	2.00	272
106	31-Oct-2017	11:12	Stream	157.8489	21.4545	0.77	10.14	0.50	6.14	6.71	3.43	306
107	31-Oct-2017	11:55	Stream	157.8419	21.4435	0.84	15.92	0.29	11.42	11.78	4.14	388
108	3-Nov-2017	7:45	Stream	157.8381	21.4475	0.39	17.56	2.00	3.50	5.64	11.92	336
109	3-Nov-2017	8:05	Stream	157.8381	21.4528	0.42	13.85	2.43	2.57	5.57	8.28	395
110	3-Nov-2017	8:25	Stream	157.8333	21.4475	0.48	100.88	2.21	39.70	42.05	58.83	388
111	3-Nov-2017	9:00	Stream	157.8433	21.4375	0.94	60.33	2.00	40.84	42.91	17.42	421
112	4-Dec-2017	11:20	Stream	157.8431	21.4667	0.81	31.84	3.93	8.00	12.07	19.78	369
113	4-Dec-2017	11:40	Porewater	157.8431	21.4667	0.39	204.90	1.36	137.79	139.50	65.40	460
114	4-Dec-2017	12:40	Stream	157.8549	21.4664	0.42	25.35	0.43	9.64	10.57	14.78	450
115	4-Dec-2017	13:35	Stream	157.8474	21.4596	0.87	220.18	4.85	72.11	77.68	--	350
116	5-Dec-2017	9:45	Ocean	157.8428	21.4683	1.03	21.13	6.50	5.85	12.49	8.64	58
117	5-Dec-2017	10:16	Porewater	157.8431	21.4679	0.74	32.63	33.56	0.14	33.77	-1.14	220
118	5-Dec-2017	10:35	Porewater	157.8443	21.4698	2.29	6.43	5.85	0.07	6.00	0.43	193
119	5-Dec-2017	10:48	Ocean	157.8442	21.4712	0.97	9.07	1.78	0.57	2.86	6.21	51
120	5-Dec-2017	11:13	Porewater	157.8445	21.4721	0.58	96.45	1.07	55.76	57.40	39.05	391
121	5-Dec-2017	11:46	Ocean	157.8424	21.4732	0.68	4.50	0.21	1.00	1.36	3.14	46
122	5-Dec-2017	11:57	Ocean	157.8430	21.4733	0.77	5.21	0.50	0.57	1.14	4.07	56
123	11-Dec-2017	12:08	Ocean	157.8283	21.4610	0.19	4.21	1.29	0.71	2.07	2.14	8

Sample No.	Date	Time	Type	X (long)	Y (lat)	Total P (uM P)	Total N (uM N)	NH_3+NH_4 (uM N)	NO_2+NO_3 (uM N)	DIN (uM N)	DON (uM N)	Si (uM)
124	11-Dec-2017	12:48	Ocean	157.8292	21.4666	0.26	5.00	1.57	0.36	2.00	3.00	8
125	11-Dec-2017	14:00	Porewater	157.8260	21.4541	1.32	13.28	13.92	0.07	14.06	-0.79	334
126	11-Dec-2017	15:02	Ocean	157.8308	21.4577	0.36	7.57	1.43	0.64	2.14	5.43	13
127	11-Dec-2017	15:40	Porewater	157.8317	21.4582	3.03	46.69	0.14	32.91	33.13	13.56	739
128	11-Dec-2017	16:04	Ocean	157.8319	21.4591	0.42	4.57	0.79	1.07	1.93	2.64	16
129	11-Dec-2017	17:24	Ocean	157.8427	21.4647	1.74	11.85	3.71	4.57	8.50	3.36	43
130	11-Dec-2017	18:12	Ocean	157.8416	21.4792	1.78	15.06	1.50	1.43	3.14	11.92	114
131	20-Dec-2017	10:50	GW	157.8419	21.4434	0.23	11.85	0.36	5.50	6.00	5.85	418
131D	20-Dec-2017	10:50	GW	157.8419	21.4434	0.29	29.06	0.36	5.71	6.50	22.56	449
132	20-Dec-2017	12:17	Ocean	157.8408	21.4608	3.55	16.49	3.71	6.64	10.71	5.78	62
133	20-Dec-2017	12:37	Stream	157.8433	21.4643	1.42	73.04	14.99	38.62	55.47	17.56	289
134D	20-Dec-2017	12:37	Stream	156.8433	22.4643	1.29	71.61	14.64	35.98	52.62	18.99	363
135	26-Dec-2017	17:20	Stream	157.8431	21.4419	1.23	70.47	0.36	10.99	11.64	58.83	203
136	1-Feb-2018	10:20	GW	157.8573	21.4558	1.42	2.28	0.29	2.71	3.07	-0.79	456
137	1-Feb-2018	11:40	GW	157.8385	21.4575	6.52	8.92	4.14	6.21	10.42	-1.50	468
137D	1-Feb-2018	12:20	GW	157.8385	21.4575	6.39	13.85	6.14	8.71	14.92	-1.07	452
138	1-Feb-2018	13:15	GW	157.8388	21.4575	4.29	354.83	296.29	0.64	297.00	57.83	287
139	1-Feb-2018	14:00	GW	157.8315	21.4292	1.84	12.07	0.14	5.21	5.43	6.64	291
140	2-Feb-2018	10:30	GW	157.8450	21.4522	1.94	9.35	0.43	9.71	10.21	-0.86	499
140D	2-Feb-2018	10:30	GW	157.8450	21.4522	1.84	10.42	0.36	9.64	10.07	0.36	437
141	25-Sep-2017	10:00	WW	157.7054	21.3388	50.25	558.61	315.23	188.89	504.12	54.49	1078
142	25-Sep-2017	10:30	WW	157.7054	21.3388	35.36	474.89	202.12	271.00	473.12	1.77	1070
143	25-Sep-2017	10:45	WW	157.7054	21.3388	151.15	3855.44	3534.70	0.38	3535.08	--	1023

Sample No.	Date	Time	Type	X (long)	Y (lat)	Total P (uM P)	Total N (uM N)	NH_3+NH_4 (uM N)	NO_2+NO_3 (uM N)	DIN (uM N)	DON (uM N)	Si (uM)
144	28-Feb-2018	10:00	Septic	157.8390	21.4576	262.86	5484.71	4620.85	0.88	4621.73	--	469
144D	28-Feb-2018	10:00	Septic	157.8390	21.4576	262.58	5606.22	4719.85	1.06	4720.91	--	500
145	28-Feb-2018	10:00	Septic	157.8390	21.4576	341.91	5878.75	5506.23	3.34	5509.57	--	389
146	28-Feb-2018	11:34	Stream	157.8418	21.4291	1.43	12.87	0.07	11.28	11.35	1.52	601
146D	28-Feb-2018	11:34	Stream	157.8418	21.4291	1.43	12.87	0.07	11.28	11.35	1.52	601
147	28-Feb-2018	11:52	Stream	157.8407	21.4298	1.12	9.86	0.06	8.67	8.73	1.13	572
148	28-Feb-2018	12:05	Stream	157.8390	21.4307	0.98	6.73	0.05	5.09	5.14	1.58	570
149	27-Apr-2018	9:00	Estuary	157.8390	21.4572	0.64	18.51	1.80	10.83	12.63	5.88	361
150	27-Apr-2018	9:10	Estuary	157.8390	21.4573	0.78	23.04	2.10	14.75	16.85	6.19	373
151	27-Apr-2018	9:30	Estuary	157.8390	21.4574	0.80	24.18	3.80	14.16	17.96	6.22	323
152	27-Apr-2018	9:40	Estuary	157.8390	21.4577	0.85	23.03	2.55	14.37	16.92	6.11	359
153	27-Apr-2018	10:30	Estuary	157.8339	21.4585	3.43	107.77	8.64	49.60	58.24	49.53	216
154	27-Apr-2018	11:00	Stream	157.8418	21.4433	0.78	21.88	0.07	16.10	16.17	5.71	452

REFERENCES

Amato, D.W., Bishop, J.M., Glenn, C.R., Dulai, H., and Smith, C.M., 2016. Impact of submarine groundwater discharge on marine water quality and reef biota of Maui, PLoS ONE, 11(11), doi: 10.1371/journal.pone.0165825.

Babcock, R.W., Lamichhane, K.M., Cummings, M.J., and Cheong, G.H., 2014. Water Science & Technology, 70.6, 1083-1089, doi: 10.2166/wst.2014.336.

Banks, W.S.L., Paylor, R.L., and Hughes, W.B., 1996. Using thermal-infrared imagery to delineate ground-water discharge, Ground Water, 34(3), 434–443.

Barlow, P.M., Cunningham, W.L., Zhai, T., Gray, M., 2015. U.S. Geological Survey Groundwater Toolbox, A Graphical and Mapping Interface for Analysis of Hydrologic Data (Version 1.0) -- User Guide for Estimation of Base Flow, Runoff, and Groundwater Recharge From Streamflow Data, Techniques and Methods, Book 3, Chapter B10.

Culbertson, C.W., Huntington, T.G., Caldwell, J.M, and O'Donnell, C.O., 2013. Evaluation of aerial thermal infrared remote sensing to identify groundwater-discharge zones in the Meduxnekeag River, Houlton, Maine, U.S. Geological Survey Open-File Report 2013-1168.

Dailer, M.L., Knox, R.S., Smith, J.E., Napier, M., and Smith, C.M., 2010. Using δ15N values in algal tissue to map locations and potential sources of anthropogenic nutrient inputs on the island of Maui, Hawai'i, USA, Marine Pollution Bulletin, 60, 655-671, doi: 10.1016/j.marpolbul.2009.12.021.

Dailer, M.L., Ramey, H.L., Saephan, S., and Smith, C.M., 2012. Algal δ15N values detect a wastewater effluent plume in nearshore and offshore surface waters and three-dimensionally model the plume across a coral reef on Maui, Hawai'i, USA, Marine Pollution Bulletin, 64, 207-213, doi: 10.1016/j.marpolbul.2011.12.004.

Danielescu, S., MacQuarrie, K.T.B., and Faux, R.N., 2009. The integration of thermal infrared imaging, discharge measurements and numerical simulation to quantify the relative contributions of freshwater inflows to small estuaries in Atlantic Canada, Hydrol. Process., 23, 2847-2859, doi: 10.1002/hyp.7383.

Donato, M.M., 1998. Surface-water/ground-water relations in the Lemhi River Basin, east-central Idaho, U.S. Geological Survey Water-Resources Investigations Report 98-4185.

Duarte, T.K., Hemond, H.F., Frankel, D., and Frankel, S., 2006. Assessment of submarine groundwater discharge by handheld aerial infrared imagery: case study of Kaloko fishpond and bay, Hawai'I, Limnol. Oceanogr.: Methods, 4, 227-236.

Dulai, H., Kleven, A., Ruttenberg, K., Briggs, R., and Thomas, F., 2016. Evaluation of submarine groundwater discharge as a coastal nutrient source and its role in coastal groundwater quality and quantity. Emerging Issues in Groundwater Resources, 187-221, doi: 10.1007/978-3-319-32008-3_8.

Engott, J.A., Johnson, A.G., Bassiouni, M., and Izuka, S.K., 2015. Spatially distributed groundwater recharge for 2010 land cover estimated using a water-budget model for the island of O'ahu, Hawai'i, U.S. Geological Survey Scientific Investigations Report 2015-5010, doi: 10.3133/sir20155010.

Faux, R.N., Lachowski, H., Maus, P., Torgersen, C.E., and Boyd, M.S., 2001. New approaches for monitoring stream temperature: Airborne thermal infrared remote sensing. Remote Sensing Applications Laboratory Project Report, U.S. Department of Agriculture Forest Service.

FAA (Federal Aviation Administration), 2016. Summary of Small Unmanned Aircraft Rule (Part 107). Online. https://www.faa.gov/uas/media/Part_107_Summary.pdf.

Giambelluca, T.W., Chen, Q., Frazier, A.G., Price, J.P., Chen, Y.-L., Chu, P.-S., Eischeid, J.K., and Delparte, D.M., 2013: Online Rainfall Atlas of Hawai'i, Bull. Amer. Meteor. Soc., 94, 313-316, doi: 10.1175/BAMS-D-11-00228.1.

Glenn, C.G., Whittier, R.B., Dailer, M.L., Dulaiova, H., El-Kadi, A.I., Fackrell, J., Kelly, J.L., Waters, C.A., Sevadjian, J., 2013. Lahaina groundwater tracer study – Lahaina, Maui, Hawaii. Final Report prepared for the State of Hawaii Department of Health, U.S. EPA, and U.S. Army Engineer Research and Development Center.

Handcock, R.N., Torgersen, C.E., Cherkauer, K.A., Gillespie, A.R., Tockner, K., Faux, R.N., and Tan, J., 2012. Thermal infrared remote sensing of water temperature in riverine landscapes, Fluvial Remote Sensing for Science and Management, John Wiley & Sons, Ltd, 85-113.

Hawai'i State Department of Health, 2015. Cesspools in Hawai'i. Joint Government Water Conference. Online. http://health.Hawai'i.gov/sdwb/files/2015/09/A02cesspooljointwaterconference-sina-bob.pdf.

Hawai'i State Department of Health, 2017. Report to the Twenty-Ninth Legislature, Relating to Cesspools and Prioritization for Replacement. Online. https://health.hawaii.gov/opppd/files/2017/12/Act-125-HB1244-HD1-SD3-CD1-29th-Legislature-Cesspool-Report.pdf.

Healy, D.F., 2003. Ground-water/surface-water relations along Honey Creek, Washtenaw County, Michigan, 2003. U.S. Geological Survey Open-File Report 2004-1387.

Hoover, D.J., 2002. Fluvial Nitrogen and Phosphorus in Hawaii: Storm Runoff, Land Use, and Impacts on Coastal Waters, PhD Dissertation, University of Hawai'i at Mānoa.

Hrudey, S.E., and Hdrudey, E.J., 2007. Published case studies of waterborne disease outbreaks – evidence of a recurrent threat, Water Environment Research, 79(3), 233-245, doi: 10.2175/106143006X95483.

Hunt, C.D., Jr., 1996. Geohydrology of the island of Oahu, Hawaii, U.S. Geological Survey Professional Paper 1412-B.

Institute of Hydrology, 1980a. Research report, v. 1 *of* Low Flow studies: Wallingford, United Kingdom, Institute of Hydrology, 42 p.

Institute of Hydrology, 1980b. Catchment characteristic estimation manual, v. 3 *of* Low flow studies: Wallingford, United Kingdom, Institute of Hydrology, 27 p.

Izuka, S.K., and Gingerich, S.B., 1998. Ground water in the southern Lihue Basin, Kauai, Hawaii, U.S. Geological Survey Water-Resources Investigations Report 98-4031.

Izuka, S.K., Engott, J.A., Bassiouni, M., Johnson, A.G., Miller, L.D., Rotzoll, K., and Mair, A., 2015. Volcanic aquifers of Hawai'i—hydrogeology, water budgets, and conceptual models, U.S. Geological Survey Scientific Investigations Report 2015-5164, doi: 10.3133/sir20155164.

Johnson, A.G., Glenn, C.R., Burnett, W.C., Peterson, R.N., and Lucey, P.G., 2008. Aerial infrared imaging reveals large nutrient-rich groundwater inputs to the ocean. Geophys. Res. Lett., 35(15), doi: 10.1029/2008GL034574.

Kelly, J.L, Glenn, C.R., and Lucey, P.G., 2013. High-resolution aerial infrared mapping of groundwater discharge to the coastal ocean, Limnol. Oceanogr.: Methods, 11, 262-277, doi: 10.4319/lom.2013.11.262.

Kennedy, J.J., 2016. Coupling aircraft and unmanned aerial vehicle remote sensing with simultaneous in situ coastal measurements to monitor the dynamics of submarine groundwater discharge, MS Thesis, University of Hawai‘i at Mānoa.

Kleven, A., 2014. Coastal groundwater discharge as a source of nutrients to Heeia Fishpond, Oahu, HI. Undergraduate Thesis, Global Environmental Science Program, University of Hawaii at Manoa.

Knobeloch, L., Saina, B., Hogan, A., Postie, J., and Anderson, H., 2000. Blue babies and nitrate-contaminated well water, Environmental Health Perspectives, 108(2), 675-678.

Lee, E., Yoon, H., Hyun, S.P., Burnett, W.C., Koh, D-C., Ha, K., Kim, D-j., Kim, Y., and Kang, K-m., 2016. Unmanned aerial vehicles (UAVs)-based thermal infrared (TIR) mapping, a novel approach to assess groundwater discharge into the coastal zone, Limnol. Oceanogr.: Methods, 14, 725-735.

Macdonald, G.A., Abbott, A.T., and Peterson, F.L., 1983. Volcanoes in the Sea, University of Hawaii Press, Honolulu.

Mayfield, K.K., 2013. A summary of the submarine groundwater discharge (SGD) in Kahana Bay: spatial and intra-daily variability. Undergraduate Thesis, Global Environmental Science Program, University of Hawaii at Manoa.

McCaul, M., Barland, J., Cleary, J., Cahalane, C., McCarthy, T., and Diamond, D., 2016. Combining remote temperature sensing with in situ sensing to track marine/freshwater mixing dynamics, Sensors, 16, doi: 10.3390/s16091402.

Moore J.G., Clague D.A., Holcomb, R.T, Lipman, P.W., Normark, W.R., Torresan, M.E., 1989. Prodigious submarine landslides on the Hawaiian Ridge, J. Geophys. Res., 94, 17,465-17,484.

Moore, J.G., Normark, W.R., Holcomb, R.T., 1994. Giant Hawaiian landslides: Annual Review of Earth and Planetary Sciences, 22,119–144, https://doi.org/10.1146/annurev.ea.22.050194.001003.

Mulligan, A.E., and Charette, M.A., 2006. Intercomparison of submarine groundwater discharge estimates from a sandy unconfined aquifer, Hydrology, 11, doi: 10.1016/j.hydrol.2005.11.056.

National Oceanic and Atmospheric Administration, 2007. Digital Elevation Models (DEMs) for the main 8 Hawaiian Islands, NOAA National Geophysical Data Center. Online. https://www.ngdc.noaa.gov/docucomp/page?xml=NOAA/NESDIS/NGDC/MGG/DEM/iso/xml/3410.xml&view=getDataView&header=none.

National Oceanic and Atmospheric Administration, 2011. Gridded bathymetry of Kaneohe Bay, Windward Side Oahu, Main Hawaiian Islands, USA, NOAA Pacific Islands Benthic Habitat Mapping Center. Online. https://www.coris.noaa.gov/metadata/records/html/kaneohe_bathy_4m.html.

National Oceanic and Atmospheric Administration, 2018. National Data Buoy Center. Online. http://www.ndbc.noaa.gov.

Novello, A., 2000. The Washington County Fair Outbreak Report, Albany, New York State Department of Health.

Oki, D.S., 2005. Numerical simulation of the effects of low-permeability valley-fill barriers and the redistribution of ground-water withdrawals in the Pearl Harbor Area, Oahu, Hawaii, U.S. Geological Survey Scientific Investigations Report 2005-5253.

Rehmel, M., 2007. Application of acoustic Doppler velocimeters for streamflow measurements, Journal of Hydraulic Engineering, 133(12), 1433-1438, doi: 10.1061/(ASCE)0733-9429(2007)133:12(1433).

Rotzoll, K., and El-Kadi, A.I., 2007. Numerical Ground-Water Flow Simulation for Red Hill Fuel Storage Facilities, NAVFAC Pacific, Oahu, Hawaii, University of Hawaii Water Resources Research Center Report.

Rotzoll, K., and El-Kadi, A.I., 2008. Estimating hydraulic conductivity from specific capacity for Hawaii aquifers, USA, Hydrogeology Journal, 16(5), 969-979, doi: 10.1007/s10040-007-0271-0.

Said, B., Wright, F., Nichols, G.L., Reacher, M., and Rutter, M., 2003. Outbreaks of infectious disease associated with private drinking water supplies in England and Wales 1970-2000, Epidemiol. Infect., 130, 469-479, doi: 10.1017/S0950268803008495.

Sherrod, D.R., Sinton, J.M., Watkins, S.E., and Brunt, K.M., 2007. Geologic Map of the State of Hawai'I, U.S. Geological Survey Open-File Report 2007-1089.

Street, J.H., Knee, K.L., Grossman, E.E., Paytan, A., 2008. Submarine groundwater discharge and nutrient addition to the coastal zone and coral reefs of leeward Hawaii. Mar. Chem., 109, 355-376, doi: 10.1016/j.marchem.2007.08.009.

Takasaki, K.J., and Mink, J.F., 1985. Evaluation of major dike-impounded ground-water reservoirs, Island of Oahu, U.S. Geological Survey Water-Supply Paper 2217.

Tamborski, J.J., Rogers, A.D., Bokuniewicz, H.J., Cochran, J.K., and Young, C.R., 2015. Identification and quantification of diffuse fresh submarine groundwater discharge via airborne thermal infrared remote sensing. Remote Sensing of Environment, 171, 202-217, doi: 10.1016/j.rse.2015.10.010.

Todd, D.K., 1980. Groundwater Hydrology, John Wiley & Sons, New York, New York, 535 p.

United States Environmental Protection Agency, 2009. National Primary Drinking Water Regulations. Online. https://www.epa.gov/sites/production/files/2016-06/documents/npwdr_complete_table.pdf.

United States Geological Survey, 1978-2018, National Water Information System: Web Interface. Online. https://waterdata.usgs.gov/hi/nwis/rt.

United States Census Bureau, 2016, United States Census Bureau QuickFacts. Online. http://www.census.gov/quickfacts.

United States Department of Agriculture, 2017, NRCS Web Soil Survey. Online. https://websoilsurvey.sc.egov.usda.gov/App/HomePage.htm.

Visher, F.N., and Mink, J.F., 1964. Ground-Water Resources in Southern Oahu, Hawaii, U.S. Geological Survey Water-Supply Paper 1778.

Walker, G.P.L., 1986. Koolau Dike Complex, Oahu: Intensity and origin of a sheeted-dike complex high in a Hawaiian volcanic edifice, Geology, 14, 310-313.

Walker, G.P.L., 1987. The Dike Complex of Koolau Volcano, Oahu: Internal Structure of a Hawaiian Rift Zone, U.S. Geological Survey Professional Paper 1350.

Whittier, R.B., and El-Kadi, A.I., 2009. Human and environmental risk ranking of onsite sewage disposal systems, Final. Prepared for the State of Hawai'i Dept. of Health by University of Hawai'i at Manoa, Dept. of Geology and Geophysics. http://health.hawaii.gov/wastewater/files/2015/09/OSDS_OAHU.pdf.